CRYSTAL GROWTH & DESIGN

pubs.acs.org/crystal

Article

Cation-/Ligand-Induced Solvent-Assisted Transformations of Zn(II) and Cu(II) Complexes Featuring Single-Pocket Multidentate Chelating Members

Siya T. Hulushe,* Frederick P. Malan,* Eric C. Hosten, Matthew P. Akerman, Andreas Lemmerer, Setshaba D. Khanye, and Gareth M. Watkins

Cite This: *Cryst. Growth Des.* 2023, 23, 4836−4854

Read Online

ACCESS | Metrics & More | Article Recommendations | Supporting Information

ABSTRACT: A new family of single-pocket metal complexes bearing O,N,O-tridentate and O,N-bidentate chelating members {Cu, **1b** ($P2_1/n$); Ni, **1c** ($C2/c$); Mn, **1d** ($I2/a$); Cu, **2b**; and Ni, **2c** (both $P2_1/c$)}, starting from synthesized and fully characterized Zn(II) (**1a**; $I2/a$) and Cu(II) (**2a**; C_2) precursors, were conveniently prepared via cation-induced solvent-assisted and ligand-induced solvent-assisted transformations. Herein, we show multistep solvent-assisted transformations from *cis*-**1a** → *trans*-**1b** → *cis*-**1c** → *cis*-**1d**, as well as all-*trans* **2a** → **2b** → **2c**. All processes are one-way irreversible, as substantiated by thermodynamic aspects (enthalpies based on Gibbs free energies) derived from density functional theory calculations. On the other hand, complex **2a′** ($C2/c$; a polymorphic form of **2a**) was obtained through a routine synthetic procedure. The compounds have been established by various spectroscopic techniques (infrared, UV−vis, ESI-MS, ^{1}H, and ^{13}C NMR), elemental analysis, and X-ray crystallography. Single-crystal X-ray studies reveal that complexes **1a**−**d** exhibit a pseudo-octahedral geometry around each metal center, with **2a** displaying a four-coordinate seesaw geometry Cu(II) sphere (Addison parameter; τ = 0.42), while **2a′** (τ = 0.00), **2b** (τ = 0.00), and **2c** (τ = 0.00) possess a perfect square-planar configuration around each metal center. Furthermore, distortion is stabilized by the presence of peripheral O-donor atoms from the bulky −OMe group, and by virtue of its size, increased bond lengths and angles are accommodated. Ligand substitution induced coordination geometry transformation from quasi-square-planar **2a** to perfect square-planar **2b**. Assessment of the metric parameter shows that the distances between the two Cu−$O_{methoxy}$ are all largely positive due to Jahn−Teller distortion, indicating an unprecedented tetragonal bipyramidal geometry in **1b**.

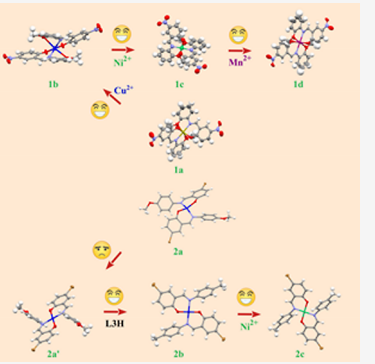

1. INTRODUCTION

Over time, the inorganic chemistry community has progressively developed many unconventional routes to devise and prepare unique inorganic systems. The major significant synthetic impediment for inorganic chemists is frequently acquiring pure chelates and bringing forth their coordination to suitable metal centers or reactive metal precursors that allow for mild reaction conditions, short reaction times, and, most importantly, high yields and product purity.[1−3] This can be accomplished, for example, by employing renowned synthetic pathways such as cation-induced solvent-assisted (CISA)[a] and ligand-induced solvent-assisted (LISA)[b] transformation reactions.[4−7] Solvent-assisted transformations render one of the most indispensable strategies for preparing novel complexes which otherwise cannot be obtained via conventional routes.[8−12] Generally, solvent-assisted transformations admit to bond breaking/formation.[13−15] As such, self-assembly transitions can be reversible[8,16] or irreversible[17−22] depending either on thermodynamic or kinetic factors governing the metal's reactivity (i.e., preferable coordination number and geometry, availability of d-orbitals, change in ionic radii, and oxidation state of the metal).[17−26] Furthermore, crystallographic transformations are highly desirable for comprehending structural changes. However, one major challenge is obtaining the crystalline phase of both the reactant and the product without crystal degradation, in which case, these solution-mediated transformations, more often than not, are accompanied by single-crystal to amorphous-phase transitions.[27,28]

The phenomenon of solution-mediated transformation has been studied long ago,[29,30] and since then, it has been paid continuous attention as evidenced by the increase in the number of publications in recent years.[31−44] Generally, redissolution and reprecipitation reactions are often exemplified by a color change which nominates multidentate chelating ligands as potential contenders for sensor technology.[45−48]

Received: January 16, 2023
Revised: May 22, 2023
Published: June 7, 2023

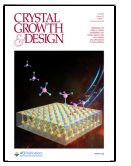

Moreover, structural transformation describes a micromutual process through which a single crystal undergoes phase transitions upon exposure to external perturbation such as temperature, pressure, or light, solvent molecules (or vapors), and seldom by employing mechanochemical forces.[49−56] Solvent-assisted post-synthetic modification (PSM) may be stimulated by ion exchange (both cation and anion). For achieving CISA-based structural transformation, a single crystal is immersed in the solution of another solid material with which the cation is substituted, and structural modifications via transmetalation are observed.[51] Direct cation exchange is usually employed in isostructure synthesis of small molecules with tractable physical properties[57−59] and is also one of the PSM pathways for designing topologically identical but functionally diverse crystalline materials.[12,60−63]

To date, a significant amount of studies have been undertaken on transmetalation; however, studies on solution-mediated transformations involving hybrids based on the combination of metal ion centers and organic ligands still remain scarce. In particular, CISA and LISA transitions relating to single-pocket (or salicylaldimine) metal complexes, despite the fact that solid-state transformations, have been known for decades. As recently as 2013, Huang et al.[64] reported metal ion-exchange reaction in a discrete $[Co(bpip)Cl_2]_2$ (where bpip = *N,N-bis*-(3-pyridyl)isophthalamide) complex to the isomorphous structure $[Hg(bpip)Cl_2]_2$ on introducing a methanolic solution of mercury(II) chloride. In addition, the latter was further transformed into a two-dimensional wavy sheet $[Cd(bpip)(SO_4)(H_2O)_2]_n$ structure when the crystals of the latter were soaked in methanolic cadmium(II) sulfate solution utilizing equimolar amounts. The cation exchange proceeds via a recurrent dissolving-exchange-crystallization phenomenon of the solvent-controlled mechanism accompanied by bond breaking and new bond formation.[65] Another recent example of inorganic systems that undergoes structural transformations for which the initial and final crystalline phases have been elucidated by single-crystal X-ray diffraction (SCXRD) includes a one-dimensional (1D) *zigzag* chain of Zn^{II}-salicylaldiminato which was investigated via metal ion exchange, and this led to the formation of a new structure in conjunction with change in the coordination environment of the Zn^{II} center.[66,67]

In few ligand substitution transformations,[68−71] a C_3-symmetry semi-rigid *N,N′,N″*-tris(3-pyridinyl)phosphoric triamide (tppa) ligand was employed to construct a discrete octahedral nanocage $[Cu_6(tppa)_8(H_2O)_6](ClO_4)_{12}(H_2O)_{24}$.[68] Upon adding NaCl solution, the non-coordinating ClO_4^- ions were substituted by bridging and non-coordinating Cl^- ions to afford a 1D polymeric[68] $[Cu_6Cl_5(tppa)(\mu\text{-}Cl)]_n(Cl)_6(H_2O)_{22}$. Essentially, this ligand-exchange reaction was abetted by structural transformation. To this end, one cannot overemphasize the importance of the aforementioned unconventional synthetic approaches in the fields of coordination and organometallic chemistry. The two classical approaches, however, concern the development of catalytic transformation by one-pot synthesis to obtain desired products in the most efficient manner.[72] Furthermore, applying synthetic control over the coordination geometry of inorganic systems is cardinal to eliciting specific physicochemical properties, and thus, synthetic routes to access unique coordination configurations create opportunities to innovate new chemical models.[73−75]

Scheme 1. Synthetic Procedure for Ligands L1H−L3H

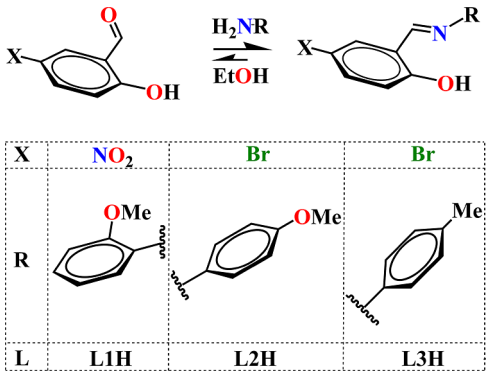

As part of the effort in studying salicylaldimine ligands (Scheme 1), herein we have made use of 5-nitro-*N*-[2-(methoxy)phenyl]salicylaldimine (**L1H**), 5-bromo-*N*-[4-(methoxy)-phenyl]salicylaldimine (**L2H**), and 5-bromo-*N*-[4-(methyl)phenyl]salicylaldimine (**L3H**) featuring O,N,O-tridentate and O,N-bidentate donor sets for the synthesis of Zn^{II} (**1a**) and Cu^{II} (**2a**) precursors by slow evaporation at room temperature (RT). A new family of metal complexes were prepared utilizing the above-mentioned precursors via CISA (Cu, **1b**; Ni, **1c**; Mn, **1d**; and Ni, **2c**) and LISA (Cu, **2b**) transformations. Notably, the crystal structure of complex **2b** is known and has been reported previously.[76] Therefore, a total of nine new compounds were elucidated by SCXRD and fully characterized by various analytic techniques. The metal(II) precursors were chosen due to their synthetic availability, versatility as synthons for other divalent metal ions such as Mn^{2+}, Ni^{2+}, and Cu^{2+}, and accordingly their ability to provide diverse geometries. On the other hand, the choice for the ligands is favorable owing to the involvement of borderline donor property of azomethine nitrogen along with a hard oxygen donor originating from the phenolato moiety to coordinate the 3d metal ions. For ligand substitution transformation, electron-withdrawing (5-Br) and electron-releasing (4-OMe, 4-Me) substituents' effect of individual ligands are the main constituents that require consideration. With this in mind, we employed **L2H** and **L3H** in LISA transformation. The aforementioned chelating derivatives exhibit very similar structures and coordination abilities but are slightly different in size. In this work, we surmise that the ligand with weak coordination capability will be substituted by the stronger one, favoring the occurrence of solution-mediated transformation. The purpose of this work is to study by experimental and computational means how the nature of the chelates can influence the overall structures of the six- and four-coordinate metal complexes.

2. RESULTS AND DISCUSSION

2.1. Synthesis and Characterizations. Schiff condensation reactions of aldehydes with 1 equiv of aromatic anilines were carried out under reflux in ethanolic solutions to afford **L1H**, **L2H**, and **L3H** (Scheme 1) in good yields (76−87%). Single crystals of the above congeners were grown by slow evaporation from different solvent systems (see the Experimental Section). The atomic numbering scheme and the anisotropic displacement parameters are depicted in Figure S1a−c (Supporting Information), and their crystal data parameters, selected bond lengths, and angles are shown in

https://doi.org/10.1021/acs.cgd.3c00055
Cryst. Growth Des. 2023, 23, 4836−4854

Scheme 2. Self-Assembly of 1a: (i) $Zn(OAc)_2{\cdot}2H_2O$, DMF/MeOH (1:1, v/v) Mixture at RT, CISA Transformations 1a → 1b: (ii) $Cu(OAc)_2{\cdot}2H_2O$, MeOH at RT; 1b → 1c: (iii) $Ni(OAc)_2{\cdot}2H_2O$, DMSO/MeCN (1:2, v/v) at RT, Destructive Transmetalation: (iv−vi) $MX_2{\cdot}xH_2O$ (M = Co^{2+} and Fe^{2+}; X = Cl^-, NO_3^-, etc.), MeOH or EtOH at RT, CISA Transformation of 1c → 1d: $Mn(OAc)_2{\cdot}4H_2O$), MeOH at RT, and Decaying of L1H → mbac: (vii) $CoCl_2$ and MeOH/THF (1:2, v/v) at RT

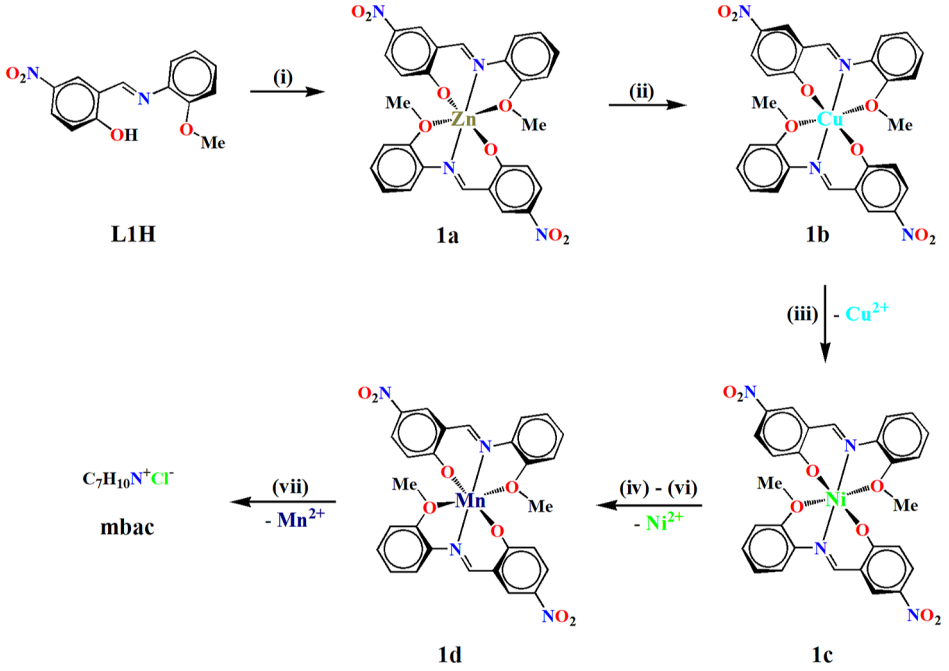

Tables S1−S5. The crystal packing in **L1H**−**L3H** is secured by various strong intermolecular interactions (Figure S2 and Table S6) between adjacent molecules bringing forth different supramolecular synthons.

To elucidate the retention of the chelates, liquid-state ^{1}H NMR experiments were performed in DMSO-d_6 solvent (Figure S3). The base peaks in the $(ESI\text{-}MS)^+$ spectra were found at m/z 273.0873, 306.0134, and 290.0182, corresponding to ($[\mathbf{L1H} + H]^+$), ($[\mathbf{L2H} + H]^+$), and ($[\mathbf{L3H} + H]^+$), respectively (Figure S4). A search of the Cambridge Crystallographic Data Centre (CCDC) 2022.3 (Cambridge Structural Database Release, November 2022)[77,78] flagged no reports of X-ray crystallographic studies on the chelating ligands presented in this work, except for **L1H** which was recently described by our group.[79]

First, to construct a *bis*(chelate) complex $[Zn(O,N,O\text{-}L1)_2]$ (*cis*-**1a**), **L1H** was treated with 0.5 equiv of Zn(II) acetate dihydrate in a DMF/MeOH (1:1, v/v) mixed solvent system at RT. Single crystals of **1a** could be obtained in 70% yield after 5 days by slow evaporation from the mother liquor (Scheme 2). After isolating the product, the ^{1}H NMR spectrum in $CDCl_3$ (Figure S3) showed the signal based on the expected C_{2v} symmetry of a Zn(II) complex. However, the imine proton undergoes an expected upfield shift from δ_H = 8.31 to ∼8.76 ppm on complexation. The absence of the phenolic proton signal (at 14.66 ppm in the free **L1H** ligand) in **1a** indicates coordination by phenolic oxygen (O1) to Zn(II) after deprotonation. The ^{1}H and ^{13}C NMR spectra conform to the structure of **1a** in agreement with elemental analyses. Electrospray ionization mass spectrometry (negative mode; ESI-MS) illustrated the presence of a mononuclear structure (observed m/z = 605.0703) which corresponds to the desired **1a** (calcd m/z = 606.0729). Moreover, C═N at 1618 cm^{-1} (Figure S5) stretching vibration of **L1H** was red-shifted to 1609 cm^{-1}, with the ν_{O-H} vibration between 3500 and 3179 cm^{-1} disappearing after metalation, again demonstrating the involvement of O1 oxygen atom with the Zn(II) center. As illustrated in Figure S6, the homogeneity of **1a** was confirmed by powder X-ray diffraction (PXRD) patterns. As expected, magnetic moment measurements (μ_{eff}) show a diamagnetic **1a**. The impetus for the synthesis of **1a** was to use this readily isolated starting material in the preparation of other coordination compounds incorporating 3d metals. However, starting from the precursor of **1a**, we were able to grow $[Cu(O,N,O\text{-}L1)_2]$ (*trans*-**1b**) after 7 days by the CISA method, and single crystals were obtained in 74% yield. This was achieved by dipping brown crystals of **1a** in a concentrated methanolic solution of $Cu(OAc)_2{\cdot}2H_2O$ (0.1 M) at RT. Unlike the reaction of **L1H** with zinc(II) acetate, complexation at ambient temperature using acetate/nitrate salts of copper(II) and manganese(II) was ineffective as was running the reaction under reflux for 2 h. Nonetheless, the positive mode ESI-MS analysis of **1b** showed a peak for the pseudo-molecular ion with m/z 606.0806 ($[\mathbf{1b} + H]^+$) and/or 628.0626 ($[\mathbf{1b} + Na]^+$), which could be rationalized by considering a mononuclear complex. When the crystals of **1b** were immersed at RT in a DMSO/MeCN (1:2, v/v) mixture of $Ni(OAc)_2{\cdot}4H_2O$, yellow-green needles of $[Ni(O,N,O\text{-}L1)_2]$ (*cis*-**1c**) were obtained after 4 days in 68% yield. The formation of the Ni(II) species, confirmed by the positive mode ESI-MS, showed a prominent peak at m/z 601.0861 corresponding to ($[\mathbf{1c} + H]^+$) (calculated m/z 600.0791). Saddle brown prisms of $[Mn(O,N,O\text{-}L1)_2]$ (*cis*-**1d**) were grown in 79% yield after 4 days in a similar manner as with **1c**, but instead a methanolic solution comprising an excess of manganese acetate tetrahydrate was utilized. The product of the above reaction displayed signals at m/z 536.1652 ($[\mathbf{1d} - (HNO_3) + H]^+$) and 557.1653 ($[\mathbf{1d} - (HNO_3) + Na]^+$) in positive mode ESI-MS.

Compounds **1a**−**d** were isolated as crystalline solids which differ in color; brown **1a** → Prussian blue **1b** → yellow-green

https://doi.org/10.1021/acs.cgd.3c00055
Cryst. Growth Des. 2023, 23, 4836−4854

Scheme 3. Self-Assembly of 2a: (i) $Cu(OAc)_2{\cdot}2H_2O$, DMF/MeOH (1:1, v/v) at RT, (ii) Refluxing $Cu(OAc)_2{\cdot}2H_2O$ and L2H in Ethanolic Solution at 80 °C for 12 h, which was then Recrystallized Using DMF/MeOH (1:1, v/v) Mixture[a]

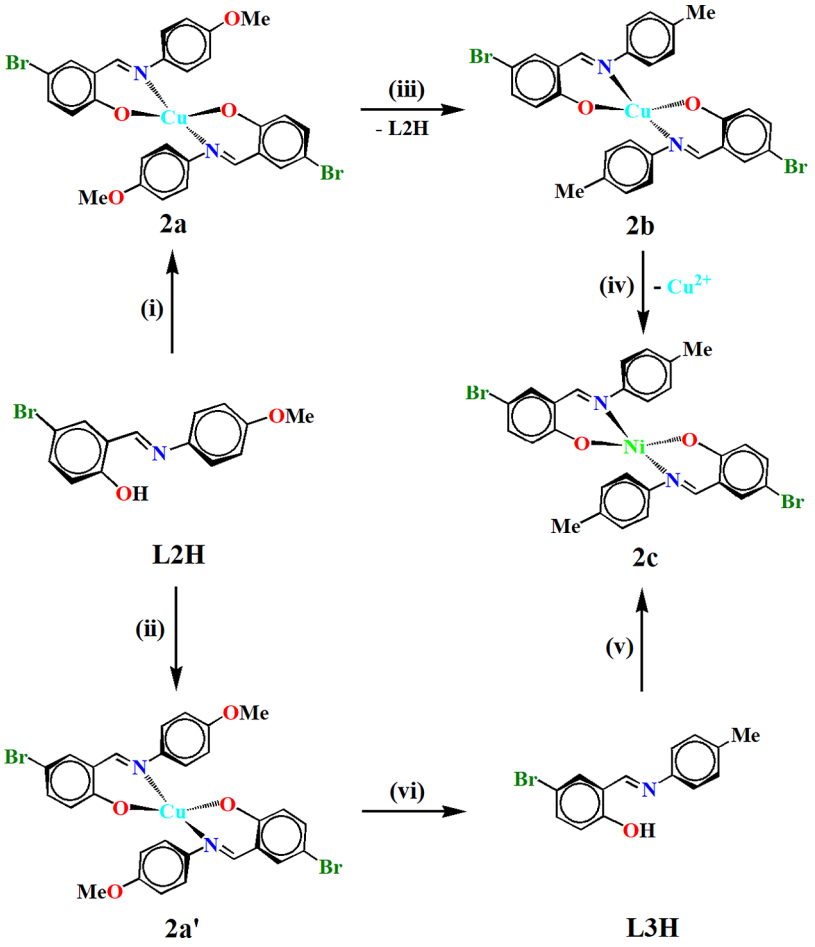

[a]Crystals of **2a′** were grown by slow evaporation at RT, (iii) LISA transformation of **2a** → **2b**, (iv) CISA transformation of **2b** → **2c**, (v) self-assembly of **2c**: refluxing $Ni(OAc)_2{\cdot}2H_2O$ and **L3H** in DMF/acetone (1:1, v/v) mixture at 70 °C, and (vi) LISA transformation was not detected.

1c → **1d** saddle brown after solution-mediated transformations. The RT magnetic moments (μ_{eff}) of complexes **1b–d** were in the range of 1.77–5.89 μ_B, corresponding to their electron configurations. As with IR spectra of **1a**, the absorption bands at 3300–3500 cm^{-1} (Figure S5) for the hydroxyl groups in the free ligand disappeared in complexes **1b–d**, suggesting the deprotonation of **L1H** and successful formation of the σ bond with the respective metal ions. Furthermore, the peaks in the range 1596–1610 cm^{-1} in their IR spectra, assigned to the stretching vibrations of the imine groups, shifted to lower frequency compared to the free ligand **L1H** (1618 cm^{-1}), indicating the coordination of the C═N groups with the metal center. The elemental analysis data (Experimental Section) is consistent with the formulation $C_{28}H_{22}N_4O_8M$ [M = Cu (for **1b**), Ni (for **1c**), and Mn (for **1d**)]. As shown in Figure S6, the PXRD patterns coincide with the structures elucidated by single-crystal diffraction data, substantiating the pure phases of **1b–d**. Our numerous attempts to isolate Co^{II} and Fe^{II} complexes containing anionic **L1** via the transmetalation route unexpectedly led either to the formation of a powdered solid (in the case of Co(II) species) or demetalation if not a complete decomposition of **L1H** to generate 2-methoxybenzenamonium chloride (designated as **mbac**; Figure S1d) salt. Significantly, metal ion exchange occurred in the same order as the ionic radii Mn > Ni > Cu > Zn. Solution UV–vis spectroscopy not only confirmed in situ one-way metal ion exchanges (see later) but also suggested geometry configurations of **1b**. In general, the electronic transitions for d^{10}-block Zn(II) and d^5-block high-spin Mn(II) complexes are spin-forbidden and hence cannot be observed. The electronic spectrum of **1b** (Figure S7) displayed absorption bands typical for octahedral geometry. The characteristic band in the visible region (at 676 nm) may be ascribed to a composite of two possible transitions $^2B_{1g} \rightarrow {}^2B_{2g}$ and $^2B_{1g} \rightarrow {}^2E_g$ out of three spin-allowed transitions of tetragonally elongated copper(II) ions with approximate D_{4h} symmetry.[80] Reduction of symmetry from pseudo-octahedral to D_{4h} is also indicated by a weak bond formed between the Cu(II) and O2 atoms of the 2-OMe groups as a consequence of distortion and high dipole moment in **1b**. The electronic spectrum of the nickel complex **1c** is also consistent with octahedral geometry displaying two d–d transitions at 690 and 392 nm assignable to $^3A_{2g}$ (F) → $^3T_{1g}$ (F) and $^3A_{2g}$ (F) → $^3T_{1g}$ (P) transitions, respectively.[81] The magnetic moment of **1c** was μ_{eff} = 3.68 BM, supporting the d^8 high-spin distorted octahedral structure.

Next, the combination of **L2H** with the copper(II) acetate dihydrate (0.5 equiv) in DMF/MeOH (1:1, v/v) solvent mixture at RT affords $[Cu(O,N\text{-}L2)_2]$ (*trans*-**2a**) crystals in 72% yield on standing for 4 days.

https://doi.org/10.1021/acs.cgd.3c00055
Cryst. Growth Des. 2023, 23, 4836–4854

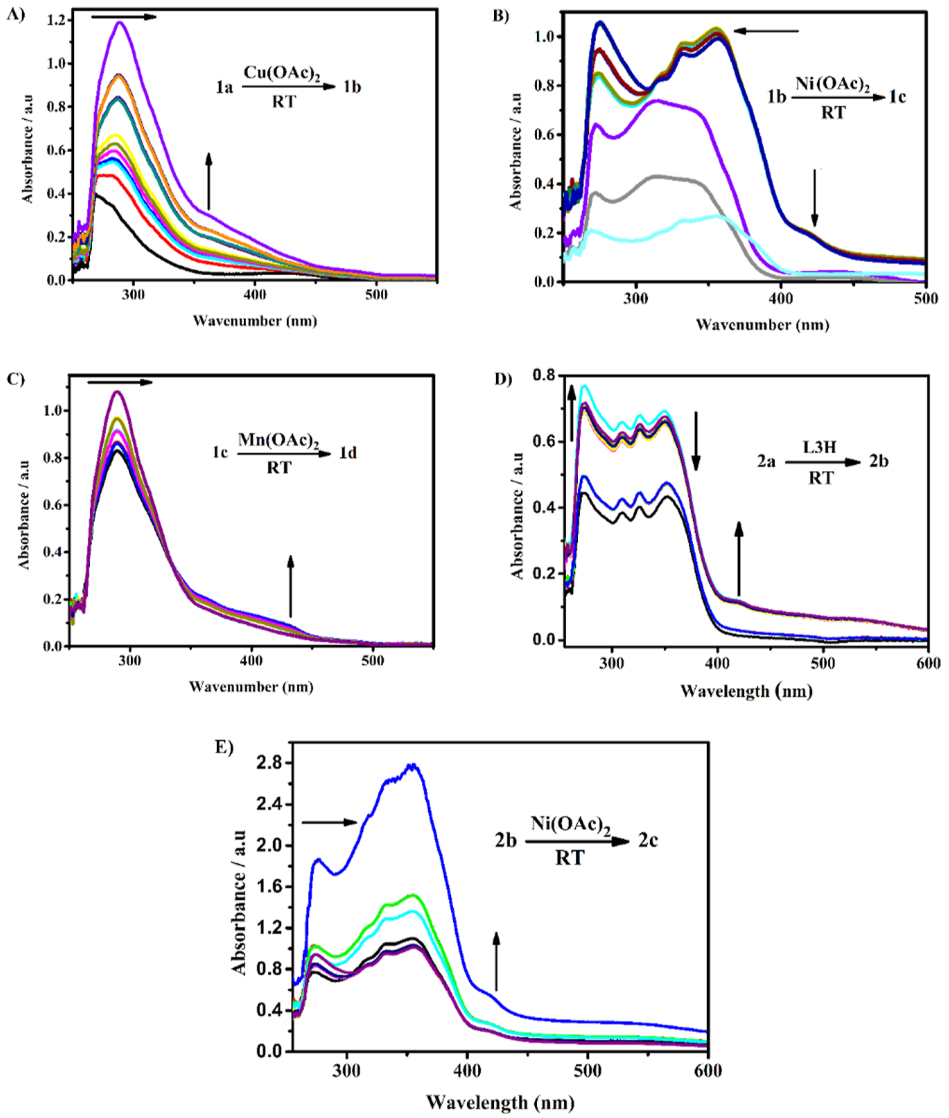

Figure 1. UV−vis spectra of (A) **1a** → **1b** after the addition of 0.1 M $Cu(OAc)_2{\cdot}2H_2O$ methanolic solution; (B) **1b** → **1c** after the addition of DMF/MeOH (1:1, v/v) solvent mixture of $Ni(OAc)_2{\cdot}2H_2O$; (C) **1b** → **1c** when a methanolic solution of $Mn(OAc)_2{\cdot}4H_2O$ was utilized; (D) **2a** → **2b** after a 1.0 M solution of **L3H** in water/DMF (2:1, v/v) mixture was introduced, and (E) **2a** → **2b** after the addition of 0.5 M $Ni(OAc)_2{\cdot}2H_2O$ in DMF/acetone (1:1, v/v) mixture. All the electronic spectra measurements were conducted at RT, and the starting times (in hrs) are presented by the colored lines: black (0), red (12), green (24), blue (36), cyan (48), pink (60), yellow (72), golden brown (84), peach (96), indigo (108), brown (120), light green (132), dark green (144), dark blue (156), orange (168), and purple (180).

Treatment of $Cu(OAc)_2$ and **L2H** gave rise to a polymorphic form of **2a** (hereafter denoted as **2a′**) as a crystalline powder after stirring under reflux for 12 h at 80 °C. The experimental and simulated PXRD patterns are imposable (Figure S6), confirming the purity of **2a′**. Dark blue crystals of **2a′** (obtained in 81% yield) were harvested by recrystallization of the crude powder from a similar solvent mixture as in the syntheses of **1a** and **2a**. Furthermore, transmetalation of Mn(II) to Zn(II) complexes from **2a** were all futile. This urged us to forge ahead with ligand substitution (Scheme 3) by dipping crystals of **2a** in a saturated methanolic solution containing **L3H** to form $[Cu(O,N\text{-}L3)_2]$ (*trans*-**2b**). As exemplified by SCXRD, **L3H** insertion induces change in geometry from quasi-square-planar *trans*-**2a** to a perfect square-planar *trans*-**2b** complex. The transformation proceeded within 6 days giving **2b** in 73% yield. Therefore, the square-planar product **2b** of a substitution reaction has a vastly different coordination environment as the reactant **2a** triggered by replacement of the departing **L2H** by the incoming **L3H** ligand. In contrast, $[Ni(O,N\text{-}L3)_2]$ (*trans*-**2c**) crystals were grown in 74% yield after 3 days in a similar manner as with **1c**, but instead, a DMF/acetone solvent system containing nickel acetate dihydrate was employed. Reaction of $Ni(OAc)_2$ solution with **L3H** at 70 °C (12 h) afforded **2c** as a light green powdered solid in 77% yield. Compound **2a** was able to undergo LISA transformation into **2b**, assisted by a stereochemical change, in a process triggered by excess **L3H**. This is a very rare case and can be characterized as an S_N2 nucleophilic ligand substitution reaction. The distorted square-planar geometry of **2a** is somewhat surprising in light of the observation of square-planar complexes **2a′**, **2b**, and **2c** for bidentate chelates. This switch in geometric preference is not immediately apparent and is certainly not a result of subtle steric interactions. On the basis of these observations, **L2H** is a significantly weaker bidentate O,N-donor chelate in comparison to **L3H** owing to the deficient electron-donating

https://doi.org/10.1021/acs.cgd.3c00055
Cryst. Growth Des. 2023, 23, 4836−4854

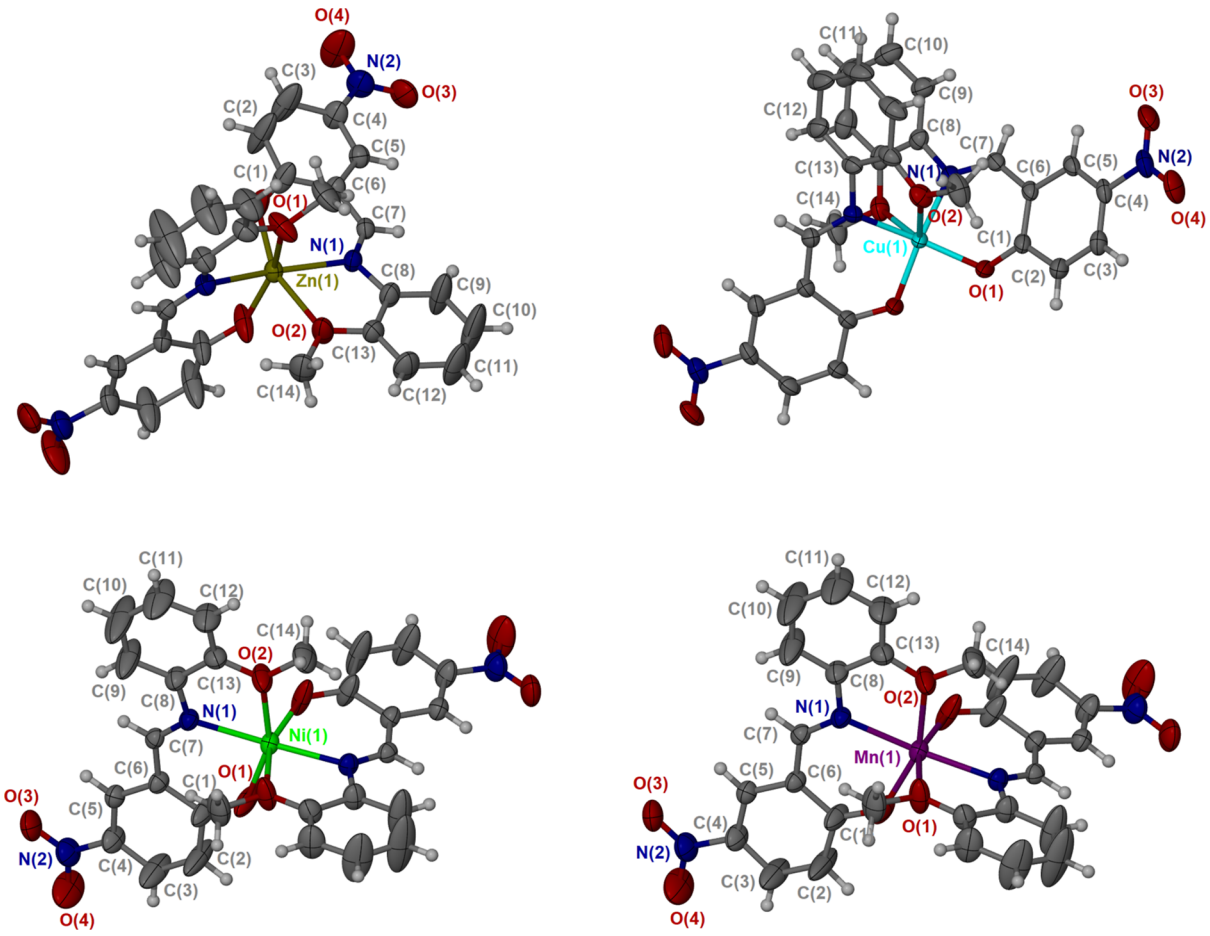

Figure 2. Molecular structures with partial atom numbering scheme of (top left) **1a** viewed down the [011] direction, (top right) **1b** viewed along the *a*-axis, and (bottom left) **1c** and (bottom right) **1d** both viewed down the *b*-axis. Ellipsoids are drawn at 50% probability. The ligand units are related by 2-fold rotation symmetry for each molecule. H atoms are shown as small gray spheres of arbitrary radii. Selected bond distances (Å) and bond angles (deg): for **1a**, Zn1−O1 1.9760(14), Zn1−O2 2.2853(15), Zn1−N1 2.0763(13), O1−Zn1−O2 163.64(6), and O1−Zn1−O1* 101.64(11). For **1b**, Cu1−O1 1.9135(13), Cu1−O5 1.8974(13), Cu1−N1 1.9959(15), O1−Cu1−O5 88.01(6), and O1−Cu1−N1 91.69(6). For **1c**, Ni1−O1 1.977(5), Ni1−O2 2.132(5), Ni1−N1 2.031(6), O1−Ni1−O2 170.10(2), and O1−Ni1−O1* 95.90(3). For **1d**, Mn1−O1 2.0329(16), Mn1−O2 2.2656(16), Mn1−N1 2.2234(16), O1−Mn1−O2 156.98(6), and O1−Mn1−O1* 100.12(14).

characteristic of the *p*-OMe (at 4-position) substituent in **2a**. Hence, the former was easily substituted by the latter via LISA transformation. While the molecular structure of **2a** (μ_{eff}: 1.88 BM) shows the *trans* configuration of the oxygen donors, both **2a′** (μ_{eff}: 1.71 BM) and **2b** (μ_{eff}: 1.68 BM) assume a square-planar environment. Also, typical solvent-assisted transformation were followed visually by the fast color change from dark blue (**2a**) → light blue (**2b**) → green for nickel(II) species **2c** with absorption of their respective $[M(O,N\text{-}L)_2]$ chromophore observed at λ_{max} = 415, 362, and 386 nm for LLCT/LMCT transition. Signals in the proton NMR spectra of **2a**, **2a′**, and **2b** complexes are very broad owing to the paramagnetic nature of the Cu^{II} ion, and hence, no further ^1H NMR analysis was performed. As shown in Figure S4, mononuclear **2a**, **2a′**, **2b**, and **2c** complexes were, respectively, assigned by ESI-MS (m/z = 669.9510 for ($[\mathbf{2a} - H]^+$), 697.9005 for ($[\mathbf{2a'} + Na]^+$), 645.9782 for ($[\mathbf{2b} + H]^+$), and 636.9355 for ($[\mathbf{2c} + H]^+$) in 48.6%, 51.4, or 100% abundance), and these molecular ion peaks are indicative for 1:2 (M/L) structures. By looking at the IR spectra of **2a**, **2a′**, **2b**, and **2c**, the formation of azomethine bonds can be verified. Namely, the IR vibration centered ±1613 cm^{-1} in **L2H**/**L3H** disappears as a new band corresponding to the chelating C═N unit emerges at 1608 cm^{-1} (for **2a**), 1605 cm^{-1} (for **2a′**), 1609 cm^{-1} (for **2b**), and 1606 cm^{-1} (for **2c**). The purity of the complexes was validated by elemental analysis and PXRD diffractograms. Agreeing with SCXRD (see crystal structure discussion later), again, the coordination environment around each metal(II) ion was also inferred by solution electronic spectra. The adsorption bands located below λ_{max} = 350 nm were ascribed to a ligand-to-metal charge-transfer (LMCT) transitions for **2a**, **2a′**, **2b**, and **2c**. The UV−vis spectra recorded in $CHCl_3$ showed an absorption band at 672 nm (assigned for $^1A_{1g} \rightarrow {}^1B_{1g}$ transition) characteristic of distorted square-planar **2a**. The electronic spectra of **2a′** and **2b** both showed two bands characteristic for square-planar configurations: at 505−508 nm (for $^2B_{1g} \rightarrow {}^2E_g$) with **2c** exhibiting a very intense spin and dipole allowed ligand-to-ligand charge-transfer (LLCT) at 700−650 nm for a typical (μ_{eff}: 0.089 BM.; diamagnetic) square-planar Ni(II) complex. Moreover, the latter two bands in **2a′** and **2b** are related to the non-resolved d−d transitions from the four low lying d-orbitals (d_{z^2}, d_{xz}, d_{yz}, and d_{xy}) to the half-filled (Cu) $d_{x^2-y^2}$ orbital.[82,83]

To gain insights into ligand exchange and Zn(II) → Cu(II), Cu(II) → Ni(II), and Ni(II) → Mn(II) (first series) and Cu(II) → Ni(II) (second series) transmetalations, UV−vis

https://doi.org/10.1021/acs.cgd.3c00055
Cryst. Growth Des. 2023, 23, 4836−4854

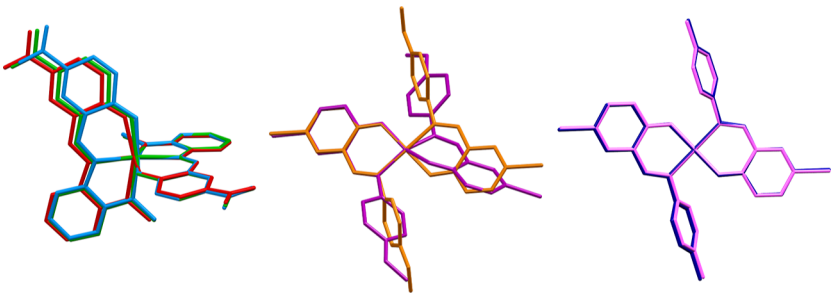

Figure 3. Molecular overlays of the crystal structures of (left): **1a** (green), **1c** (blue), and **1d** (red) with rms = 0.0751; (green and red) and 0.0768 (green and blue); (middle): **2a** (purple) and **2a′** (bronze) with rms = 0.0198; (right): **2b** (royal blue) and **2c** (pink) with rms = 0.045. All rms values calculated are based on the structure overlays of pairs of complexes with the same atoms (where possible): **1a**, **1c**, and **1d**: O1, N1, O2, and M1 (M = Zn, Ni, and Mn); **2a** and **2a′**: O1, N1, and Cu1; and **2b** and **2c**: O1, N1, and M1 (M = Cu and Ni).

aliquot sampling at 12 h intervals were recorded. Consequently, UV−vis experiments at RT were performed by removing stoichiometric volumes (∼2 μL) from the reaction mixtures, and accordingly, the samples were further diluted (10-fold) in $CHCl_3$. In the $Cu(OAc)_2$ aliquot sampling experiment, a profound bathochromic shift is observed from the absorption band at 283 nm in **1a** to 289 nm in **1b**, accompanied by an increased absorption intensity in the lower energy band (left in Figure 1A) as well as the color variation from brown to reddish-orange for the reaction mixture. Notably, an absorption band at 269 nm in **1a** disappears with a new band emerging at 362 nm in **1b** (right in Figure 1A) after 96 h.

Concerning the nickel complex **1c**, the color of the solution immediately changed from green to purple upon the addition of the $Mn(OAc)_2$ methanolic solution, while for those comprising copper(II), the solutions preserve their initial blue tint, with both **1b** and **2b** solutions turning (after 36 and 48 h, respectively) from pale blue to blue-green upon insertion of Ni^{2+} ions. Except for the continuously increasing shoulder at 428 nm, no changes were observed in the d−d transition bands for $Mn(OAc)_2$-directed Ni(II) → Mn(II) transmetalation (Figure 1C). However, solvent-assisted transformations of **1a** → **1b**, **1b** → **1c**, and **1c** → **1d** were confirmed later by their solid-state structures.

During the formation of **2b** from **2a** in solution, the intensity of the absorption bands at 274 nm (left in Figure 1D) increased, while the band at 352 nm is hypochromic (middle in Figure 1D) and with a new band appearing at 420 nm (right in Figure 1D), indicating the transformation of one species into another. The change in intensity in the latter two absorption bands are arguably ascribed to the disappearance of the uncoordinated OMe oxygen species during **2a** → **2b** transmetalation. In the UV region, the distinguishable band underwent a slightly bathochromic shift from 273 nm in **2b** to 276 nm in **2c** (left in Figure 1E) upon the addition of $Ni(OAc)_2$ solution, with broad and narrow hyperchromic absorption bands (middle and right in Figure 1E, respectively) presenting minimal hypochromic shifts, suggesting **2b** → **2c** transformation.

Following the geometric moieties realized between chelates **L2H** and **L3H** with Cu^{2+}, we rationalized that Zn^{2+}, with a slightly larger ionic radius, would institute similar outcomes. However, after multiple trials, this reaction was not feasible. Furthermore, an attempt to synthesize the analogous cobalt(II) complex from [Cu(O,O,N-L1)$_2$] (**1b**) in the presence of $Co(OAc)_2{\cdot}4H_2O$ solution led to demetalation and isolation of single crystals of **L2H**. By careful analysis of the transformation phenomenon, three specific points were noticed: (1) **1a** → **1b** → **1c** → **1d** self-assembly occurred much faster than **2a** → **2b** → **2c**, (2) the transformations take place only when metal acetates (numerous attempts were performed with the nitrates, sulfates, and bromides/chlorides without success) are utilized, and (3) all the transformation processes are irreversible. Consequently, solid-state-to-solid-state transformations involved permanent cleavage of old metal−ligand bonds and formation of new metal−ligand bonds. The kinetics for metal ion exchange of Zn(II) by Cu(II), Cu(II) by Ni(II), Ni(II) by Mn(II), and finally Cu(II) by Ni(II) were monitored by AAS. Nearly, 50% of the M(II) ions in the complexes were replaced within 5 days (in **1b**), 2.5 days (in **1c**), 1.5 days (in **1d**), and 2 days (in **2c**). In addition, 99% of the M(II) ions were exchanged between 3 and 7 days (Figure S8 and see the Experimental Section for further details). We also studied the behavior of a reverse ion exchange by soaking **1b** crystals in a methanolic solution of $Zn(OAc)_2{\cdot}2H_2O$ (0.1 M) at RT for 2 weeks. Expectedly, the ion-exchange process did not occur. Similarly, transmetalation processes were irreversible for **1d** → **1c** → **1b**, **2b** → **2a**, and **2c** → **2b**. In addition, "diagonal" transmetalation reactions (i.e., **1a** → **1c**, **1a** → **1d**, **1b** → **1d**, and **2a** → **2c**) were tried to no avail. We are currently investigating the exchange behavior of **1a**−**2c** metal ions with other 3d metal ions, in attempt to elucidate the factors that govern the metathesis reaction reported herein.

Diagrammatic representations (50% probability ellipsoids) of the crystal structures of **1a**−**d** are depicted in Figure 2 with selected bond lengths and bond angles. Compound **1c** crystallizes in the *C*2/*c* (no. 15) space group with $Z = 4$, while both **1a** and **1d** are shown to crystallize in the monoclinic *I*2/*a* (no. 5) space group with virtually identical lattice constants, and their cell volumes are 98.84% similar. The superposition (Figure 3) of the compounds shows that the two *C*2-symmetry compounds are isostructural. From the structural view point, each metal(II) center in **1a**, **1c**, and **1d** is six-coordinate composed of four O donors arising from two monoanionic (**L1**$^-$) units in a bidentate manner via phenolato O1 and methoxy O2 atoms to form a square-planar CuO_4 coordination core with two axial sites occupied by N1 and N1* donors (N1−Zn1−N1* 161.14(8)°, N1−Ni1−N1* 170.30(3)°, and N1−Mn1−N1* 163.38(9)° for the former and latter, respectively), completing the octahedral geometry. The neutral mononuclear complex **1b** crystallizes in the space group $P2_1/n$ (no. 14) and $Z = 4$. Furthermore, the highly distorted square-planar [Cu(O1, O2, O5, and O6)] subunit

https://doi.org/10.1021/acs.cgd.3c00055
Cryst. Growth Des. 2023, 23, 4836−4854

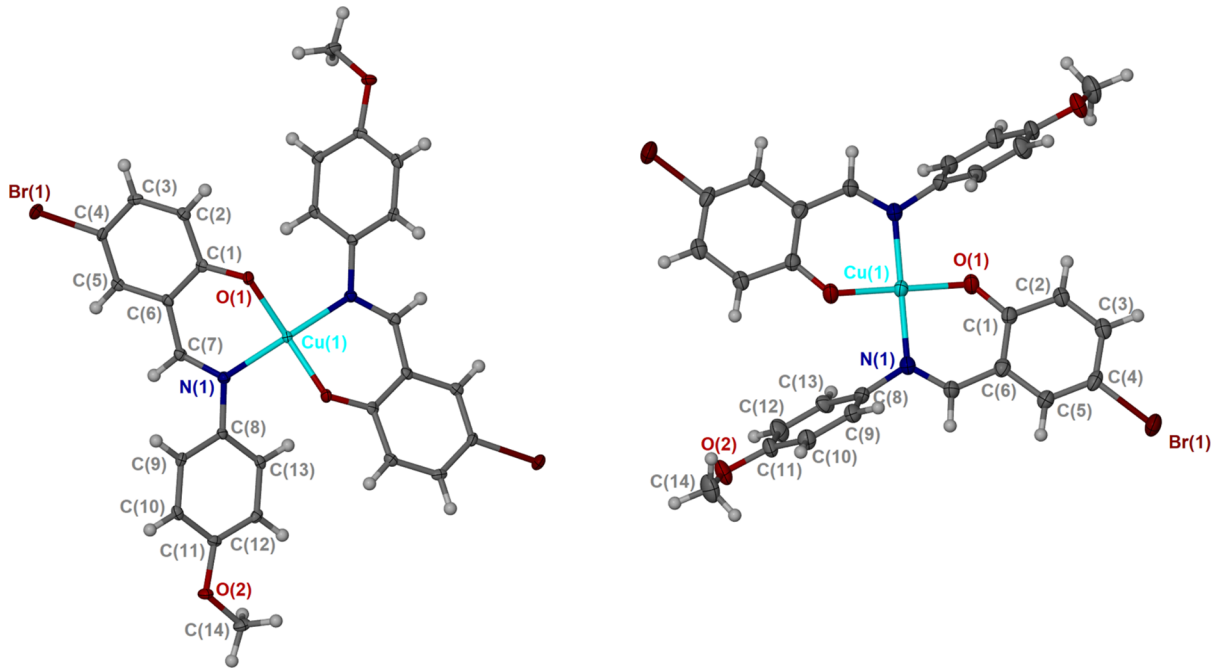

Figure 4. Molecular structures with the partial atom numbering scheme of (left) **2a** viewed down the *b*-axis and (right) **2a′** viewed along the [111] plane. Ellipsoids are drawn at 50% probability. The ligand units are related by 2-fold rotation symmetry for each molecule. H atoms are shown as small gray spheres of arbitrary radii. Selected bond distances (Å) and bond angles (deg): for **2a**, Cu1−O1 1.8826(18), Cu1−N1 2.000(2), O1−Cu1−O1* 149.47(16), and O1−Cu1−N1 93.13(9). For **2a′**, Cu1−O1 1.8915(4), Cu1−N1 2.001(4), O1−Cu1−O1* 180.00, and O1−Cu1−N1 91.30(18).

has a *trans*-form (O1−Cu1−O5 88.01(6) and N1−Cu1−N3 98.57(6)° in the basal position), in contrast to a *cis*-configuration (O1−Zn1−O1* 101.64(11)° for **1a**, O1−Ni1−O1* 95.90(3)° for **1c**, and O1−Mn1−O1* 100.15(8)° for **1d**). The distortion of the octahedral geometry is understood with the above-mentioned bond angles or at least their halves, and in this case, all deviate from the ideal values of 90° (for *cis* angles) or 180° (for *trans* angles). Within the O,N,O tridentate pocket around the 3d center in **1b**, the $Cu^{II}-N_{imine}$ distances are different at 1.9959(15) and 1.9703(15) Å, $Cu^{II}-O_{phenolate}$ are 1.9135(13) and 1.8974(14) Å, while the $Cu^{II}-O_{methoxy}$ distances are notably longer measuring 2.7102(14) and 2.6769(14) Å due to the presence of a bulky OMe group, forming an overall pseudo-octahedral CuO_4N_2 coordination core. Coordination of the Cu(II) ions in **1b** led to severe strain on the commonly planar CuO_4 center. This strain is driven by the deviation of the ligand backbone from ideal planarity, which gave rise to serious distortion leading to an unprecedented geometry around the Cu(II) center. Close inspection of the coordination environment indicate that the Cu(II) sphere forms a tetragonal plane based on O1,O1*, N1,O2*, and bipyramidal geometry appears from axial existence of two donor sites, N1* and O2. Most copper(II) complexes with Jahn−Teller distortion[84,85] undergo elongation of the *z*-axis and consequently provide an exceptional thermodynamic stability.[86,87] Similarly, the geometry of the Cu1 atoms in **1b** is somewhat an elongated octahedral; the axial M1−O1 bond lengths are 1.9760(14) Å (for **1a**), 1.977(5) Å (for **1c**), and 2.0329(16) Å (for **1d**), which are noticeably longer than those of the four equatorial bonds of **1b** as presented in the notation of Figure 2. It should be pointed out that the $M^{II}-O_{phenoxido}/M^{II}-N_{imido}$ distances follow the order **1d** > **1c** > **1a** > **1b**. Contrarily, the O1−M1−O2 bond angles for **1a**, **1b**, **1c**, and **1d** are 163.64(6), 127.31(5), 170.10(2), and 156.98(6)°, respectively, indicate that the tension of the chelate from the phenolato and azomethine groups follows the sequence **1c** > **1a** > **1d** > **1b**.

The crystal packing view of complexes **1a**, **1c**, and **1d** is very similar; therefore, only packing properties of **1a**, which are comparably different from the packing features of **1b**, are presented and discussed (Figure S9; see the Supporting Information for details).

The structural motifs of the two polymorphs are identical, with slight differences in the unit cell parameters conceivably owing to differences in symmetry. Interestingly, the two polymorphs **2a** and **2a′** were identified based on their crystal form. Both structures are monoclinic, but one crystallizes in a chiral space group *C*2 (no. 5), with Flack parameter[88] at 0.019(10), indicating that the absolute structure is correct, and the other in the space group *C*2/*c* (no. 15). The asymmetric units contain one metal ion on a special position, two anionic ligands (L^-), and with no lattice or coordinated water molecules. The crystal structures of complexes **2a** and **2a′** are shown in Figure 4 together with selected bond distances and angles. Despite the obvious differences in packing (Figure S10), the asymmetric units of the two polymorphic structures almost perfectly overlap (middle of Figure 3). Symmetry expansion reveals metal ions with four-coordinate geometries (a seesaw geometry—an intermediate conformation between tetrahedral and square planar with a calculated Addison parameter[89,90] τ = 0.42 in **2a**, while **2a′** features a perfect square-planar configuration with τ = 0.00), and the coordination spheres are occupied with two phenoxido O1 and O1* atoms as well as two iminido N1 and N1* atoms. Unexpectedly, the M−O and M−N bond distances in **2a** are slightly shorter and longer, respectively, than those in **2a′**. In **2a**, the $M-O_{phenoxido}$ and $M-N_{iminido}$ distances are 1.8834(12) and 2.0040(3) Å, respectively, while in **2a′**, they are 1.8915(4)

https://doi.org/10.1021/acs.cgd.3c00055
Cryst. Growth Des. 2023, 23, 4836−4854

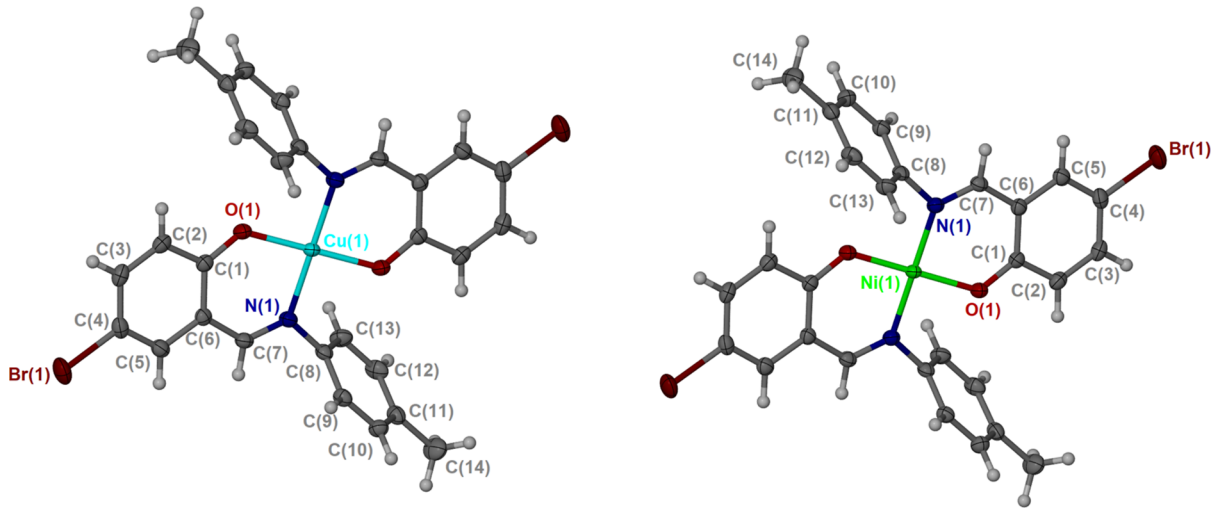

Figure 5. Molecular structures with the partial atom numbering scheme of (left) **2b** and (right) **2c** both viewed along the *a*-axis. Ellipsoids are drawn at 50% probability. The ligand units are related by 2-fold rotation symmetry for each molecule. H atoms are shown as small gray spheres of arbitrary radii. Selected bond distances (Å) and bond angles (deg): for **2b**, Cu1−O1 1.8883(16), Cu1−N1 2.0047(18), O1−Cu1−O1* 180.00, and O1−Cu1−N1 91.31(7). For **2c**, Ni1−O1 1.8349(16), Ni1−N1 1.9132(18), O1−Ni1−O1* 180.00, and O1−Ni1−N1 92.54(7).

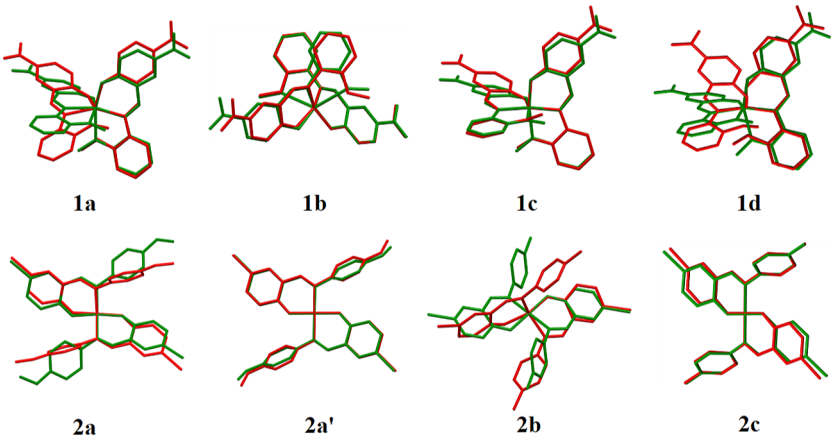

Figure 6. Molecular overlays of the solid-state structures (SCXRD) in dark green and the theoretical optimized structures (DFT) in dark red. Hydrogen atoms are omitted for clarity.

and 2.001(4) Å in the same order. However, the bond distances are slightly different from the corresponding value (1.895(2) Å) presented in a recently reported analogous Cu(II) complexes.[91−93]

The bond angles O−Cu−O and N−Cu−O are comparable and vary from 93.11(1) to 151.38(1)° in **2a** and 88.74(16) to 180.0° in **2a′**. Compounds **2b** and **2c** are isostructural; their analogy is discussed. As can be seen in the superposition of the molecular structures (right of Figure 3), there is almost an unnoticeable difference in the periphery between the two complex molecules. However, after inserting Ni^{2+} into **2b**, one can note a very slight decrease in the length of the *c*- and *b*-axes and an increase in the *a*-axis length. As illustrated in Figure 5, the asymmetric unit of the two complexes contains one half-molecule with the other half generated by an inversion center, which lies at the midpoint of the copper(II) and nickel(II) atoms. Coordination geometry of the two metal atoms can be described as a square planar with Cu1 (τ = 0.00) and Ni1 (τ = 0.00) atoms forming two six-membered chelate rings related to each other by the 2-fold rotation axis passing through the metal. As in **2a′**, the ligands in **2b** and **2c** adopt a κ^2 N/O coordination mode via the imine nitrogen and phenolate oxygen atoms. Consequent with a square-planar geometry, the metal center in the two structures are surrounded by equidistant Cu−O 1.8883(16) Å and Ni−O 1.8349(16) Å]. The O and N donor atoms are positioned *cis* to each other. In **2b**, the Cu1−O1 and Cu1−N1 distances are slightly different from the corresponding values (1.884(2)−1.887(2) Å) reported in the literature.[91,94−96] The Ni−O and Ni−N bond distances in **2c** are, however, slightly longer than the corresponding bond lengths for the previously reported nickel *bis*(bidentate) molecular complex (Ni−O 1.829(10) and Ni−N 1.909(12) Å).[97] Quite expectedly, the complementary sum of the O1−M−N1 and N1−M−O1 angles at the metal centers [91.31(7) and 88.69(7)° in **2b**] and [92.54(7) and 87.46(7)° in **2c**] are perfectly averaged to 90°. The packing features of **2b** and **2c** are thoroughly described in the Supporting Information.

3. COMPUTATIONAL STUDY

A DFT study of the various complexes has been conducted in order to gain more insights into the effects the different ligands **L1H**−**L3H** have on the geometry, electronic structure, and ligand substitution trends of the resulting complexes. In

https://doi.org/10.1021/acs.cgd.3c00055
Cryst. Growth Des. 2023, 23, 4836−4854

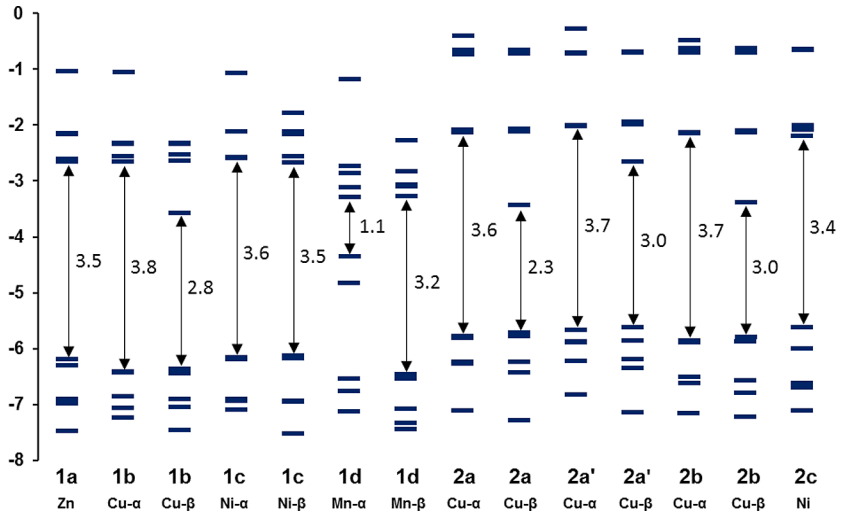

Figure 7. Orbital correlation diagram (in eV) of the d-electron occupancy for the complexes **1a**−**d** and **2a**−**c**. The black lines separate occupied orbitals (lower lying) from the unoccupied orbitals (higher lying). Corresponding energy gaps (eV) are indicated next to each blue line.

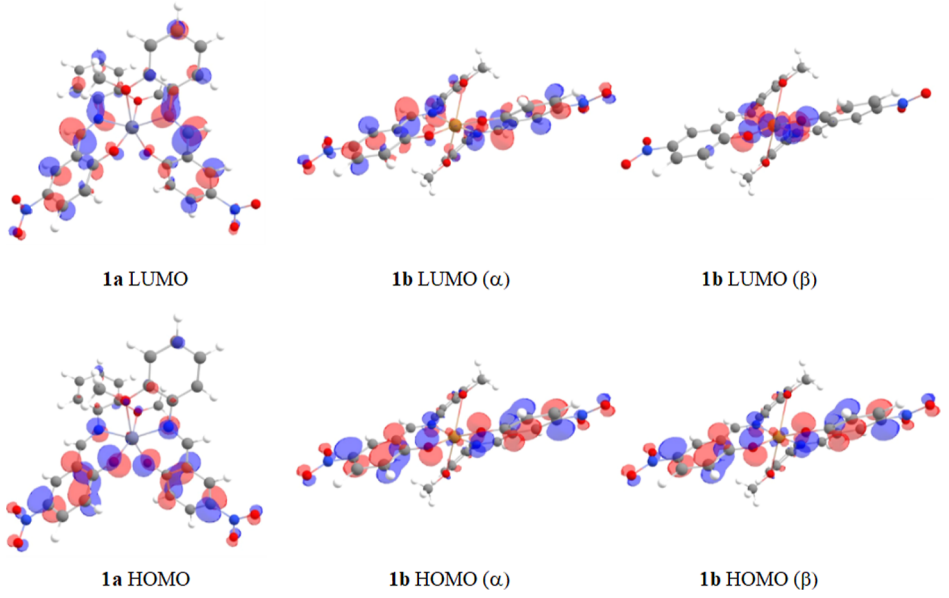

Figure 8. Graphical representation of the frontier orbitals of complexes **1a**−**b**. Color code for atoms: Zn (blue-gray), Cu (brown), N (blue), C (gray), O (red), and H (white).

general, the computed geometries correlated with the experimental (SCXRD) geometries with rms values between 0.010 and 0.144 (Figure 6). The major outliers were those of **2a** and **2b**, where the (distorted) square-planar Cu(II) complexes were obtained experimentally, in contrast to the computationally derived (highly) distorted square-planar (**2a**) and tetrahedral (**2b**) geometries (spin multiplicity of 2 for Cu^{2+}). The calculated distorted square-planar/tetrahedral geometries were also around 142 kJ mol^{-1} lower in energy as compared to the experimental square-planar counterpart. Solid-state packing effects are thought to be the major cause for the difference in geometries. The other outlier was complex **1d**, where in general, one of the coordinated ligands folded away from the ideal 90° angle between all adjacent coordinating atoms. Both spin multiplicities (2 and 6) were considered for Mn^{2+} in the low and high spin cases, respectively. However, the result from the sextet multiplicity (high spin) was chosen as the experimental properties of the complex corresponded best to the case of the highly paramagnetic complex. Considering the experimental and calculated M−O and M−N bond lengths, these also mostly corresponded well, apart from complex **1d** (Figure S12, Supporting Information).

Here, the calculated average Mn−O and Mn−N bond lengths were consistently between 0.21 and 0.35 Å shorter than the corresponding experimentally measured bond lengths. The calculated bond lengths of **1c** (spin multiplicity 2, low spin case) deviated further from the corresponding experimental bond lengths. The thermodynamics of each of the reactions to form **1b**, **1c**, **2b**, and **2c** was also evaluated using reaction enthalpy (ΔH) calculations based on the Gibbs free energies. The enthalpy of formation for each compound is calculated as the sum of the Gibbs Free energies of the products, less than the sum of the Gibbs free energies of the reactants. The formation enthalpies (based on Gibbs free energies) in the first series of reactions (i.e., **1a** → **1b** → **1c** → **1d**) are as follows:

https://doi.org/10.1021/acs.cgd.3c00055
Cryst. Growth Des. 2023, 23, 4836−4854

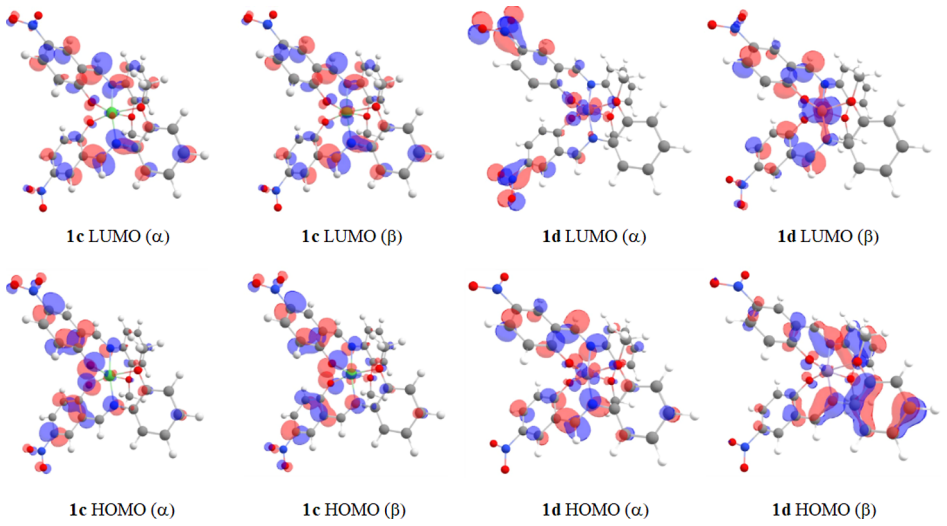

Figure 9. Graphical representation of the frontier orbitals of complexes **1c** and **1d**. Color code for atoms: Ni (green), Mn (pale lilac), N (blue), Br (maroon), C (gray), O (red), and H (white).

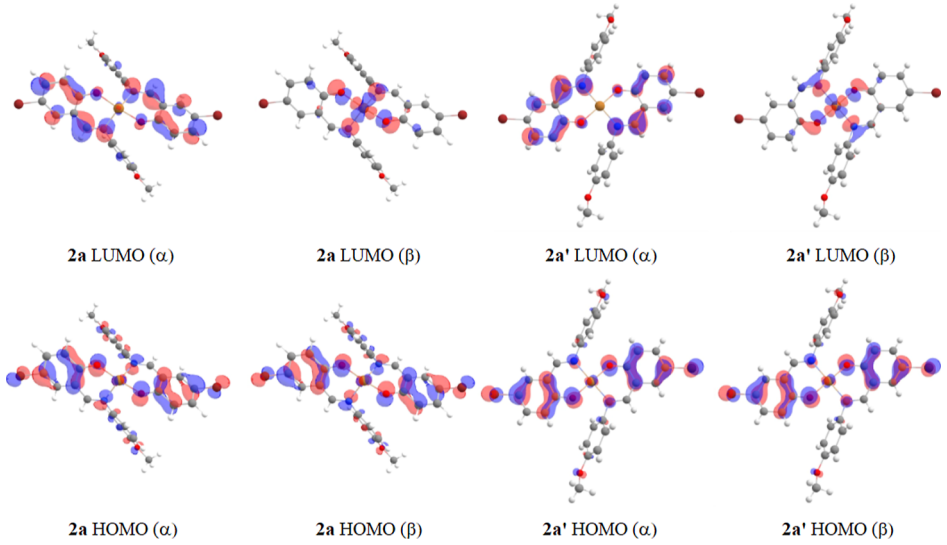

Figure 10. Graphical representation of the frontier orbitals of complexes **2a** and **2a′**. Color code for atoms: Cu (brown), N (blue), Br (maroon), C (gray), O (red), and H (white).

−10.3 kJ mol^{-1} to form **1b**, −345.6 kJ mol^{-1} to form **1c**, and −5.20 kJ mol^{-1} to form **1d**).

This finding suggests the reverse series of reactions to be energetically unfavorable (in general, and within computational error). When considering the second series of reactions, the reaction of **2a** to form **2b** is unfavorable with a positive formation enthalpy of 460 kJ mol^{-1} and is largely based on the conversion from the more stable tetrahedral (experimentally observed, theoretically predicted) to the less stable square-planar geometry. If the reaction of **2a′** to form **2b** is considered instead, it becomes favorable with −9.8 kJ mol^{-1} (square planar → square-planar geometry). Conversion of **2b** to **2c** is predicted to be favorable with a formation enthalpy of −12.6 kJ mol^{-1}. The effect of the d-electron contribution to the molecular orbitals of the different metals belonging to complexes **1a**−c and **2a**−**c** is shown in Figure 7. The depiction of the corresponding frontier orbitals of each of the complexes is shown in Figures 8 and 9. The variation of metal−ligand bond lengths may be rationalized by considering a balance of the electronic contributions to the bonding and antibonding orbitals, as well as the noticeable level of metal/ligand orbital mixing throughout the series of complexes.[98]

All complexes (apart from **1a** and **2c**) exhibited both α- and β-electron contributions, as can be seen in Figures 7−11. The last five occupied orbitals of the Zn complex (d^{10}) are fully filled and resembles that of an octahedral field. Removal of one electron to form the d^9 Cu complex (**1b**) results in a distorted octahedral field with a degree of Jahn−Teller distortion due to the asymmetrical occupation of the e_g orbitals.

This manifests as elongated apical Cu−O_{ether} bonds, as compared to the shorter Cu−O_{oxo} basal bonds. This is of course not the case in the Ni^{2+} (d^8) complex of **1c**: the (experimental) Ni−OMe bonds are the shortest of the series (1.98 Å from XRD and 1.99 Å from DFT) from which the overall geometry correlates well with the Zn^{2+} congener (**1a**). In the case of the Mn complex (**1d**), a high-spin sextet multiplicity leads to α-spin-filled orbitals, in which case is largely based on d-metal and π-ligand orbitals. Moving over to the four-coordinate complexes **2a**−**c**, the electron distribution resembles that of a distorted square-planar field, with the

https://doi.org/10.1021/acs.cgd.3c00055
Cryst. Growth Des. 2023, 23, 4836−4854

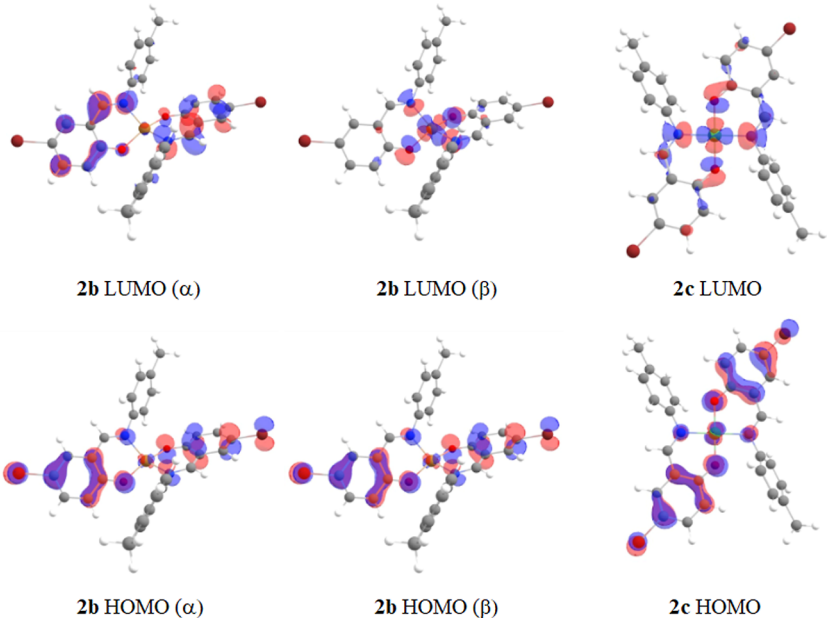

Figure 11. Graphical representation of the frontier orbitals of complexes **2b** and **2c**. Color code for atoms: Cu (brown), Ni (green), N (blue), Br (maroon), C (gray), O (red), and H (white).

nickel-based complex **2c** exhibiting a formal square-planar field of which a noticeable contribution from the d-metal orbitals is observed. Considering the α-spin electron contribution of complexes **1a**–**d**, an energy gap of 3.53 eV (Zn, **1a**) increases to 3.76 eV (Cu, **1b**) and then decreases back to 3.56 eV (Ni, **1c**). For the transformation of **1c** → **1d**, the energy gap sharply decreased to 1.05 eV (Mn, **1d**; 3.19 eV energy gap from β-spin contribution), suggesting enhanced reactivity (or lowered stability) of **1d** as compared to **1a**–**c**. In the series **2a**–**c**, the energy gap of Cu-based **2a** and **2a′** (3.65 eV in each case) slightly increases to 3.70 eV (Cu, **2b**), which in turn decreases to 3.43 eV (Ni, **2c**), suggesting similar complex reactivities and/or stabilities.

4. CONCLUSIONS

Herein, we surmise that the lower stability of single-pocket Zn(II) and Cu(II) complexes that make possible the *cis*-**1a** (Zn) → *trans*-**1b** (Cu) → *cis*-**1c** (Ni) → *cis*-**1d** (Mn), **2b** (Cu) → **2c** (Ni) transmetalations, and **2a** (Cu) → **2b** (Cu) ligand substitution. The unit cell parameters changed significantly from **1a** → **1b** → **1c** → **1d** transmetalations but just slightly from **2b** → **2c**. In the one-way irreversible solvent-assisted transformations, the cleavage of coordinative bonds and the subsequent distortion are influenced by the −OMe substituent regardless of their position (*ortho*- or *para*) on the aniline ring. The one-way directionality of the transformations was confirmed experimentally as well as computationally (DFT) by means of the calculated reaction enthalpies based on the corresponding Gibbs free energies. Furthermore, the Jahn–Teller and steric effect accompanied by the 2-OMe substituent is responsible for a significant distortion observed in **1b**. However, a substitution of the 4-OMe group by the 4-Me functionality of the O,N-donor chelate considerably influenced relaxation of distortion from an unprecedented tetrahedral bipyramidal **2a** to a perfect square-planar **2b**. In addition, **2a** → **2b** solvent-assisted transformation is possible because **L3H** exhibits a stronger ligand field than **L2H** as explicated by shorter metal–ligand bonds and larger bite angles in **2b**. The significant new advance of this work lies in the successfully in situ metal ion exchange and ligand substitution reactions of metal complexes bearing relatively large and rigid multidentate ligands. The current solvent-assisted transformation studies could provide new approaches to the selective preparation of metal complexes and further insights into mechanistic pathways that could lead to preferable geometries around coordination spheres and their physicochemical properties. This means that metal ion exchange within the context of coordination compounds may serve as a very efficient way of controlling the formation of new inorganic systems with different structure topologies. Additionally, single crystals that possess CISA and LISA transformations show great promise for application to advance adsorption and switching materials, selective chemosensors, or smart actuators.

5. EXPERIMENTAL SECTION

5.1. Reagents and Starting Materials. Chemicals used were obtained from the following sources: acetate salts of zinc(II), copper(II), manganese(II), nickel(II), and cobalt(II) and 5-bromosalicylaldehyde, 5-nitrosalicylaldehyde, *o*-anisidine, *p*-anisidine, and *p*-toluidine from Sigma-Aldrich (Pty) Ltd and Merck (Pty) Ltd with >95% chemical purity; $CDCl_3$ and DMSO-d_6 (deuterated NMR solvents) from Sigma-Aldrich (Germany) with >98% chemical purity; acetonitrile (MeCN) from Ranbaxy Fine Chemicals Ltd (India) of high-performance liquid chromatography grade; acetone, dimethylformamide (DMF), and ethanol (EtOH) from Protea Chemicals (South Africa); chloroform ($CHCl_3$) from BM Scientific/Parow Industria (South Africa); and methanol (MeOH) from Merck (Germany). All reagents and solvents were purchased from commercial sources and used without further purification.

Melting points (for ligands) were determined on a Reichert Hot-Stage (Protea Holdings Ltd.) melting point apparatus and uncorrected.

Carbon, hydrogen, and nitrogen (CHN) analysis (the sample was used as is) was performed on an Elementar Analysensysteme vario MICRO V1.6.2 GmbH analysis system. Atomic absorption spectroscopy (AAS) results (for Zn, Cu, Ni, and Mn determination using respective $MCl_2{\cdot}2H_2O$ (acquired from Sigma-Aldrich) as standards for calibrations, λ = 213.857, 324.754, 232.003, and 279.482 nm),

https://doi.org/10.1021/acs.cgd.3c00055
Cryst. Growth Des. 2023, 23, 4836−4854

Table 1. Crystal Data Parameters of Complexes 1a−d

complex	1a	1b	1c	1d
empirical formula	$C_{28}H_{22}N_4O_8Zn$	$C_{28}H_{22}N_4O_8Cu$	$C_{28}H_{22}N_4O_8Ni$	$C_{28}H_{22}N_4O_8Mn$
F. W. (g mol^{-1})	607.86	606.03	601.20	597.45
T (K)	296.0(2)	150.0(2)	100.0(2)	150.0(2)
crystal size (mm^3)	0.31 × 0.27 × 0.17	0.30 × 0.29 × 0.11	0.37 × 0.20 × 0.19	0.40 × 0.26 × 0.19
crystal color	brown	Prussian blue	yellow-green	saddle brown
lattice	monoclinic	monoclinic	monoclinic	monoclinic
space group	$I2/_a$ (no. 15)	$P2_1/n$ (no. 14)	$C2/c$ (no. 15)	$I2/a$ (no. 15)
a (Å)	12.6990(6)	10.7901(3)	20.0280(2)	12.6868(2)
b (Å)	11.9496(7)	9.7115(2)	11.8199(15)	12.0187(2)
c (Å)	17.4447(9)	24.7822(5)	12.6842(15)	17.2434(3)
β (deg)	97.930(3)	100.031(2)	121.514(4)	99.721(2)
vol. (Å^3)	2621.9(2)	2557.18(10)	2559.90(5)	2591.50(8)
Z, Z'	4, 1/2	4, 1	4, 1/2	4, 1/2
D_{calcd} (g cm^{-3})	1.540	1.574	1.560	1.531
$F(000)$	1248.0	1244.0	1240.0	1228
μ (mm^{-1})	0.997	0.916	0.819	4.670
no. reflns.	23403	47601	31946	18248
data/restr./par.	3269/0/187	7013/0/372	1660/0/187	2551/0/187
R(int)/R(sigma)	0.0492/0.0282	0.0396/0.0284	0.1390/0.0413	0.0320/0.0156
GOF[a]	1.056	1.025	1.262	1.112
R_1/wR_2 ($I > 2\sigma(I)$)[b]	0.0328/0.0842	0.0372/0.0926	0.0600/0.1424	0.0384/0.1060
R_1/wR_2 [all data][c]	0.0431/0.0897	0.0559/0.1000	0.1171/0.2086	0.0396/0.1068
max./min. (e Å^{-3})	0.34/−0.18	0.59/−0.35	1.18/−0.65	0.33/−0.32

[a]GOF = $\{\Sigma[w(F_o^2 - F_c^2)^2]/(n-p)\}^{1/2}$. [b]$R_1 = \Sigma||F_o| - |F_c||/\Sigma|F_o|$. [c]w$R_2 = \{\Sigma[w(F_o^2 - F_c^2)^2]/\Sigma[w(F_o^2)^2]\}^{1/2}$, where $w = 1/[\sigma^2(F_o^2) + (aP)^2 + bP]$, $P = (F_o^2 + 2F_c^2)/3$.

Table 2. Crystal Data Parameters of Complexes 2a−c

complex	2a	2a′	2b	2c
empirical formula	$C_{28}H_{22}N_2O_4Br_2Cu$	$C_{28}H_{22}N_2O_4Br_2Cu$	$C_{28}H_{22}N_2O_2Br_2Cu$	$C_{28}H_{22}N_2O_2Br_2Ni$
F. W. (g mol^{-1})	673.85	673.85	641.85	637.00
T (K)	100.0(2)	100.0(2)	100.0(2)	150.0(2)
crystal size (mm^3)	0.16 × 0.10 × 0.04	0.24 × 0.11 × 0.09	0.32 × 0.31 × 0.28	0.41 × 0.33 × 0.19
crystal color	dark blue	dark blue	light blue	green
lattice	monoclinic	monoclinic	monoclinic	monoclinic
space group	$C2$ (no. 5)	$C2/c$ (no. 15)	$P2_1/c$ (no. 14)	$P2_1/c$ (no. 14)
a (Å)	23.0466(15)	22.5171(17)	9.9365(9)	10.0479(15)
b (Å)	3.9565(3)	10.1586(7)	10.4339(9)	10.2768(15)
c (Å)	17.4279(11)	12.5589(10)	12.1834(10)	12.0513(18)
β (deg)	129.935(3)	116.276(2)	102.221(3)	102.040(5)
vol. (Å^3)	1218.51(15)	2575.9(3)	1234.51(19)	1217.0(3)
Z, Z'	2, 1/2	4, 1/2	2, 1/2	2, 1/2
D_{calcd} (g cm^{-3})	1.837	1.738	1.727	1.738
$F(000)$	670.0	1340.0	639.6	636.0
μ (mm^{-1})	4.216	3.988	2.218	4.110
no. reflns.	10895	11240	26008	87207
data/restr./par.	3182/1/170	3135/0/170	3046/0/160	2493/0/161
R(int)/R(sigma)	0.0307/0.0467	0.0672/0.0607	0.0737/0.0379	0.0508/0.0121
GOF[a]	1.018	1.041	1.057	1.274
R_1/wR_2 ($I > 2\sigma(I)$)[b]	0.0243/0.0436	0.0572/0.1376	0.0276/0.0610	0.0200/0.0616
R_1/wR_2 [all data][c]	0.0270/0.0444	0.0925/0.1670	0.0411/0.0695	0.0266/0.0807
max./min. (e Å^{-3})	0.51/−0.41	1.24/−1.37	0.44/−0.46	0.35/−0.38
Flack parameter	0.019(10)			

[a]GOF = $\{\Sigma[w(F_o^2 - F_c^2)^2]/(n-p)\}^{1/2}$. [b]$R_1 = \Sigma||F_o| - |F_c||/\Sigma|F_o|$. [c]w$R_2 = \{\Sigma[w(F_o^2 - F_c^2)^2]/\Sigma[w(F_o^2)^2]\}^{1/2}$, where $w = 1/[\sigma^2(F_o^2) + (aP)^2 + bP]$, $P = (F_o^2 + 2F_c^2)/3$.

were obtained employing a Varian 1275 spectrometer with a laminar acetylene burner.

Magnetic susceptibilities (Bohr Magneton; BM) of the mononuclear transition metal complexes were measured by the Gouy method at RT using the MKI Johnson Matthey model, Alfa Products, UK, a magnetic susceptibility balance, using $Hg[Co(SCN)_4]$ as a calibrant. Diamagnetic corrections for each complex were estimated using Pascal's constants. Effective magnetic moments were determined from the expression $\mu_{eff} = 2.88\ (\chi_M T)^{1/2}$, where χ_M is

https://doi.org/10.1021/acs.cgd.3c00055
Cryst. Growth Des. 2023, 23, 4836−4854

the molar magnetic susceptibility corrected for diamagnetism of the constituting atoms.

High-resolution mass spectrometry was performed on a Waters Synapt G2 TOF instrument with an ESI source, ESI Pos, Cone Voltage 15 V.

^{1}H and ^{13}C NMR spectral data were collected using a Bruker AVANCE III HD 400 MHz NMR spectrometer with tetramethylsilane as an internal reference. Spectra were recorded in deuterated solvents: all chemical shift values are reported in parts per million (ppm) referenced to residual solvent resonances ($CDCl_3$ δ_H 7.26, δ_C 77.36; DMSO-d_6 δ_H 2.50, δ_C 39.5).

Infrared (IR) spectra were collected on a PerkinElmer Spectrum 100 spectrometer with a KBr beam splitter and fitted with an attenuated total reflection (ATR) attachment. Mid-infrared spectra with a frequency of 4000−650 cm^{-1} (note: br—broad, m—medium, sh—shoulder, s—strong, and w—weak) were obtained by placing samples on a diamond/ZnSe crystal plate.

Ultraviolet−visible (UV−vis) spectra were recorded on a PerkinElmer UV−vis spectrophotometer model LAMBA 25. The compounds were dissolved in either chloroform ($CHCl_3$) or *N*,*N*′-dimethylformamide (DMF) with concentration approximately ≈0.4 mM.

Thermogravimetric (TG) measurements were carried out on a PerkinElmer TG-4000 (Pyris Version 4.01 software) at 10 °C min^{-1} heating rate with a mass between 2 and 5 mg, purging with nitrogen gas at 20 mL min^{-1}.

PXRD patterns were collected on a Bruker D8 ADVANCE diffractometer with monochromatic Cu Kα (λ = 1.54184 Å) radiation and the 2θ range of 5−60° at RT.

5.2. Single-Crystal X-ray Crystallography. All single crystals were picked under the microscope, leapt in cryo-oil or paratone oil, and mounted in a nylon loop, and all geometric and intensity data were taken from one single crystal. Datasets were collected on a Rigaku XtaLAB Synergy R/Bruker D8 VENTURE with a Photon III detector diffractometer equipped with graphite monochromated Mo Kα (λ = 0.71073 Å)/Cu Kα (λ = 1.54184 Å), with a rotating-anode X-ray source. Data reduction and absorption were carried out using the CrysAlisPro (version 1.171.40.23a)[99]/Bruker program SAINT[100] software packages. Data were collected for absorption effects using either multiscan or numerical absorption correction SADABS,[101] and the structures were solved by the direct methods package SHELXS/SHELXT-2018/2 (ref 102) or SIR-97 (refs 103 and 104) and refined using SHELXL-2018/3 (ref 105) or Olex2 (version 1.2) software incorporating SHELXL.[106] The final anisotropic full-matrix least-squares refinement was done on F^2. All non-hydrogen atoms were refined anisotropically, while all hydrogen atoms were placed in idealized positions and refined using riding models. Crystallographic data for all the complexes are given in Tables 1 and 2. Programs: PLATON[107,108] (for structure validation and geometrical calculation), Mercury,[109] and X-Seed[110] were utilized for molecular graphics and refinements, while enCIFer[111] was employed for CIF editing.

5.3. Computational Chemistry. All calculations were carried out using density functional theory (DFT) incorporating the B3LYP-D3 (B3LYP with the Grimme empirical dispersion correction D3) hybrid functional,[112,113] as implemented in the Gaussian 16 package.[114] The triple-ζ basis set def2-TZVPP[115] was used for all atoms. The geometries of all compounds were fully optimized without any symmetry restrictions, ensuring that the local minima had zero imaginary vibrational frequencies and to provide the thermal correction to free energies at 298.15 K and 1 atm. For the reaction enthalpy calculations, since there are two reactants (R) and two products (P), the free energy of the reaction in the liquid state is calculated as $\Delta G^0_{298} = (G^0_{298}(P1) + G^0_{298}(P2)) - (G^0_{298}(R1) + G^0_{298}(R2))$. For a given reactant or product, the free energy is calculated as $G^0_{298} = E + G^0_{trans} + G_{rot} + G_{vib} + G_{con}$, where G^0_{trans}, G_{rot}, G_{vib}, and G_{con} are, respectively, the translational, rotational, vibrational, and conformational free energies and E = Born−Oppenheimer energy at the equilibrium structure. The conformational energy between the reactants and products in each reaction cancel as little to no change in the ligand conformation is observed, so G_{con} is omitted. Solvent-based corrections were made for calculations using the polarizable continuum model[116] that uses the integral equation formalism variant[117] as implemented in Gaussian 16 with MeOH (ε = 32.613) as a solvent. All energies used and reported in this work are zero point vibrational-corrected. Frontier orbital density plots were generated using Chemcraft[118] using an isovalue of 0.05.

5.4. General Procedure for the Synthesis of L1H, L2H, and L3H. A mixture of aldehyde (10 mmol), amine (1 equiv), and EtOH (25 mL) was heated to reflux for 2 h in a 100 mL round-bottom flask equipped with a mechanical stirrer bar and a water-cooled condenser.

*5.4.1. 5-Nitro-N-[2-(methoxy)phenyl]salicylaldimine (**L1H**).* Upon cooling the reaction mixture, a red-orange precipitate formed, and it was then filtered off, washed with cold MeOH (10 mL × 3), dried under vacuum, and recrystallized from a saturated $CHCl_3$/water (2:1, v/v) solvent mixture. Red needles suitable for SCXRD analysis were obtained by slow evaporation after 8 days. Yield: 1.22 g (73%). mp 192 °C. IR ν_{max} (ATR) (ν, cm^{-1}): 3500−3179(br), 3055(w), 1618(s), 1555(s), 1464(m), 1313(s), 1177(s). UV−vis λ_{max} (nm) (ε, M^{-1} cm^{-1}) ($CHCl_3$): 365 (1593), 289 (1681), 271 (1728). NMR ($CDCl_3$, 400 MHz) ^{1}H 3.88 (s, 3H), 6.95−7.00 (m, 3H), 7.24−7.28 (t, J = 8.2 Hz, 2H), 8.15−8.18 (d, J = 12.0 Hz, 1H), 8.30−8.31 (d, J = 2.8 Hz, 1H), 8.74 (s, 1H), 14.66 (s, 1H); ^{13}C 57.1, 112.3, 117.5, 118.8, 120.0, 122.1, 128.9, 129.7, 134.9, 139.9, 153.5, 160.1, 169.7. HRMS (ESI) (positive mode, m/z): calcd for $C_{14}H_{12}N_2O_4$, 272.0797; found, 273.0873 ([M + H]$^+$). Anal. Calcd for $C_{14}H_{12}N_2O_4$: (%) C, 61.76; H, 4.44; N, 10.3. Found: C, 61.64; H, 4.29; N, 10.6.

*5.4.2. 5-Bromo-N-[4-(methoxy)phenyl]salicylaldimine (**L2H**).* Upon cooling the reaction mixture, a green precipitate formed, and it was then filtered off, washed thrice with 25% EtOH−water, dried under vacuum, and recrystallized from a saturated MeOH/$CHCl_3$ (2:1, v/v) solvent mixture. Yellow-green needles suitable for SCXRD grew after 4 days. Yield: 1.47 g (83%). mp 168 °C. IR ν_{max} (ATR) (ν, cm^{-1}): 3018(s), 1612(s), 1558(s), 1481(m), 1169(s). UV−vis λ_{max} (nm) (ε, M^{-1} cm^{-1}) ($CHCl_3$): 408 (2906), 356 (5632), 309 (5792), 277 (7116). NMR (DMSO-d_6, 400 MHz) ^{1}H 3.40 (s, 3H), 7.66−7.72 (d, J = 24.0 Hz, 3H), 7.86 (s, 1H), 7.99−8.01 (d, J = 8.0 Hz, 3H), 8.94 (s, 1H), 13.23 (s, 1H); ^{13}C 56.3, 110.5, 114.5, 119.5, 121.8, 128.4, 129.3, 129.7, 130.5, 134.0, 136.6, 161.6. HRMS (ESI) (positive mode, m/z): calcd for $C_{14}H_{13}BrNO_2$, 305.0051; found, 306.0134 ([M + H]$^+$). Anal. Calcd for $C_{14}H_{12}BrNO_2$: (%) C, 54.92; H, 3.95; N, 4.58. Found: C, 54.86; H, 3.89; N, 4.63.

*5.4.3. 5-Bromo-N-[4-(methyl)phenyl]salicylaldimine (**L3H**).* The synthetic procedure was the same as the method of **L2H** to afford a yellow solid which was then filtered off, washed thrice with 25% EtOH−water, dried under vacuum, and finally recrystallized from a saturated EtOH solution. Yellow needles suitable for SCXRD grew after 5 days. Yield: 1.75 g (87%). mp 175 °C. IR ν_{max} (ATR) (ν, cm^{-1}): 3012(s), 1613(s), 1559(s), 1497(m), 1174(s). UV−vis λ_{max} (nm) (ε, M^{-1} cm^{-1}) ($CHCl_3$): 397 (2944), 355 (6246), 285 (6010), 281 (7160). NMR ($CDCl_3$, 400 MHz) ^{1}H 3.77 (s, 3H), 6.83−6.90 (m, 3H), 7.42−7.33 (m, 2H), 8.46 (s, 1H), 13.38 (s, 1H); ^{13}C 55.6, 110.4, 114.7, 119.2, 120.8, 122.4, 133.9, 135.2, 140.8, 158.8, 159.2, 160.0. HRMS (ESI) (positive mode, m/z): calcd for $C_{14}H_{13}BrNO$, 289.0102; found, 290.0182 ([M + H]$^+$). Anal. Calcd for $C_{14}H_{12}BrNO$: (%) C, 57.95; H, 4.17; N, 4.83. Found: C, 58.04; H, 4.11; N, 4.77.

2-Methoxybenzenaminium chloride (**mbac**) is a serendipitous product from decaying **L1H** (note: a comparable structure (with CCDC refcode **XIGMAC**) has already been published).[119] HRMS (ESI) (positive mode, m/z): calcd for $C_7H_{10}ClNO$, 161.0421; found, 162.0528 ([M + H]$^+$). Anal. Calcd for $C_7H_{10}ClNO$: (%) C, 52.67; H, 6.31; N, 8.78. Found: C, 52.61; H, 6.27; N, 8.83.

5.5. Preparation of 1a, 2a, and 2a′. To a stirred **L1H**/**L2H** (10 mmol) in 30 mL of DMF/MeOH (1:1, v/v) solvent mixture was added $M(OAc)_2{\cdot}2H_2O$ in 0.5 equiv (M = Zn, **1a**; and Cu, **2a**) at RT. The mixture was left under continuous stirring for 1 h. The resulting solution was filtered, and crystals were grown by slow evaporation from the mother liquor in air at RT. In another experiment, a well-stirred ethanolic solution of $Cu(OAc)_2{\cdot}2H_2O$ (5 mmol) and **L2H** (2.0 equiv) was refluxed for 12 h at 80 °C. Consequently, the formed

https://doi.org/10.1021/acs.cgd.3c00055
Cryst. Growth Des. 2023, 23, 4836−4854

green powder of **2a′** was recrystallized in the DMF/MeOH (1:1, v/v) solvent mixture, and the crystals were grown by slow evaporation at RT.

*5.5.1. cis-Bis[2-({[2-(methoxy)phenyl]imino-κN}methyl)-4-nitrophenolato-κ²O,O]-zinc(II) (**1a**).* After 5 days, brown block-like crystals suitable for SCXRD were collected by filtration and washed with a very small amount of MeCN. Yield: 79.7 mg (70%). mp >273.54 °C. IR ν_{max} (ATR) (ν, cm^{-1}): 3061(s), 1609(s), 1559(w), 1514(m), 1497(m), 1305(s), 1241(s). NMR ($CDCl_3$, 400 MHz) ^1H 2.11 (s, 6H), 7.48−7.52 (t, J = 16.0 Hz, 2H), 7.89−7.93 (t, J = 16.0 Hz, 1H), 8.76−8.77 (d, J = 4.00 Hz, 2H). HRMS (ESI) (negative mode, m/z): calcd for $C_{28}H_{22}N_4O_8Zn$, 606.0729; found, 605.0703 ($[M - H]^+$). Anal. Calcd for $C_{28}H_{22}N_4O_8Zn$: (%) C, 55.32; H, 3.65; N, 9.22; Zn, 10.8. Found: C, 55.25; H, 3.59; N, 9.36; Zn, 11.3. μ_{eff} = 0.0 BM (diamagnetic).

*5.5.2. trans-Bis[2-({[4-(methoxy)phenyl]imino-κN}methyl)-4-bromophenolato-κO]-copper(II) (**2a**).* Dark blue blocks suitable for SCXRD were obtained directly after 4 days. Yield: 83.8 mg (72%). mp >270.33 °C. IR ν_{max} (ATR) (ν, cm^{-1}): 3056(s), 1608(s), 1561(s), 1498(m), 1243(s), 1016(s). UV−vis λ_{max} (nm) (ε, M^{-1} cm^{-1}) ($CHCl_3$): 672 (109), 402 (1185), 370 (1624), 306 (3162). HRMS (ESI) (negative mode, m/z): calcd for $C_{28}H_{22}Br_2N_2O_4Cu$, 670.9242; found, 669.9510 ($[M - H]$)$^+$. Anal. Calcd for $C_{28}H_{22}Br_2N_2O_4Cu$: (%) C, 49.91; H, 3.29; N, 4.16; Cu, 9.43. Found: C, 49.82; H, 3.19; N, 4.18; Cu, 9.28. μ_{eff} = 1.88 BM.

(**2a′**): Dark blue prisms suitable for SCXRD were harvested after 5 days. Yield (93.9) (81%). mp >291.65 °C. IR ν_{max} (ATR) (ν, cm^{-1}): 3059(s), 1605(s), 1558(s), 1501(m), 1246(s), 1018(s). UV−vis λ_{max} (nm) (ε, M^{-1} cm^{-1}) ($CHCl_3$): 505 (941), 357 (5853), 318 (5047), 276 (5480). HRMS (ESI) (positive mode, m/z): calcd for $C_{28}H_{22}Br_2N_2O_4Cu$, 670.9401; found, 697.9005 ($[M + Na]^+$). Anal. Calcd for $C_{28}H_{22}Br_2N_2O_4Cu$: (%) C, 49.91; H, 3.29; N, 4.16; Cu, 9.43. Found: C, 49.87; H, 3.22; N, 4.22; Cu, 9.19. μ_{eff} = 1.71 BM.

5.6. 1a → 1b CISA Transformation. The crystals of **1a**, after being washed with a small amount of MeCN, were dipped in a solution of respective $Cu(OAc)_2{\cdot}2H_2O$ (0.1 M) in a methanolic solution at RT. During this period, the solution was replaced with a fresh solution at least twice. After 7 days, the solution was decanted, and the exchanged Prussian blue block-like crystals of **1b** were washed thoroughly with MeCN.

*5.6.1. trans-Bis[2-({[2-(methoxy)phenyl]imino-κN}methyl)-4-nitrophenolato-κ²O,O]-copper(II) (**1b**).* Yield: 1.63 g (74%). mp >289.01 °C. IR ν_{max} (ATR) (ν, cm^{-1}): 3067(s), 1596(s), 1512(s), 1495(m), 1303(s), 1239(s). UV−vis λ_{max} (nm) (ε, M^{-1} cm^{-1}) ($CHCl_3$): 676 (104), 352 (2202), 325 (2935), 308 (2655), 277 (3056). HRMS (ESI) (positive mode, m/z): calcd for $C_{28}H_{22}N_4O_8Cu$, 605.0734; found, 606.0806 ($[M + H]^+$) or 628.0626 ($[M + Na]^+$). Anal. Calcd for $C_{28}H_{22}N_4O_8Cu$: (%) C, 55.49; H, 3.66; N, 9.24; Cu, 10.5. Found: C, 55.54; H, 3.60; N, 9.29; Cu, 9.89. μ_{eff} = 1.77 BM.

5.7. 1b → 1c CISA Transformation. The complex **1c** was prepared using the same procedure as described for **1b**; DMSO/MeCN (1:2, v/v) mixture of $Ni(OAc)_2{\cdot}2H_2O$ was employed instead. After 4 days, the solution was decanted, and the exchanged yellow-green needles of **1c** were washed thoroughly with cold MeOH.

*5.7.1. cis-Bis[2-({[2-(methoxy)phenyl]imino-κN}methyl)-4-nitrophenolato-κ²O,O]nickel(II) (**1c**).* Yield: 1.47 g (68%). mp >262.75 °C. IR ν_{max} (ATR) (ν, cm^{-1}): 1605 (s), 1495(m), 1515 (s), 1316 (s), 1253 (s). UV−vis: λ_{max} (nm) (ε, M^{-1} cm^{-1}) ($CHCl_3$): 690 (4870) (n−π^*), 359 (4990) (n−π^*). HRMS (ESI) (positive mode, m/z): calcd for $C_{28}H_{22}N_4O_8Ni$, 600.0791; found, 601.0861 ($[M + H]^+$). Anal. Calcd for $C_{28}H_{22}N_4O_8Ni$: C, 55.94; H, 3.69; N, 9.32; Ni, 9.76%. Found: C, 55.89; H, 3.64; N, 9.38; Ni, 9.54%. μ_{eff} = 3.68 BM.

5.8. 1c → 1d CISA Transformation. The complex **1d** was prepared using the same procedure as described for **1b**; a methanolic solution of $Mn(OAc)_2{\cdot}4H_2O$ was employed instead. After 4 days, the solution was decanted, and the exchanged saddle brown block-like crystals of **1d** were washed thoroughly with MeCN.

*5.8.1. cis-Bis[2-({[2-(methoxy)phenyl]imino-κN}methyl)-4-nitrophenolato-κ²O,O]manganese(II) (**1d**).* Yield: 0.51 g (79%). mp >161.71 °C. IR ν_{max} (ATR) (ν, cm^{-1}): 3061(s), 1610(s), 1509(s), 1480(w), 1459(m), 1305(s), 1239(w). HRMS (ESI) (positive mode, m/z): calcd for $C_{28}H_{22}N_4O_8Mn$, 597.0818; found, 536.1652 ($[M - (HNO_3) + H]^+$) or 557.1653 ($[M - (HNO_3) + Na]^+$). Anal. Calcd for $C_{28}H_{22}N_4O_8Mn$: (%) C, 56.29; H, 3.71; N, 9.38; Mn, 9.20. Found: C, 56.36; H, 3.65; N, 9.35; Mn, 9.03. μ_{eff} = 5.89 BM.

5.9. 2a → 2b LISA Transformation. *5.9.1. trans-Bis[2-({[4-(methyl)phenyl]imino-κN}methyl)-4-bromophenolato-κO]-copper-(II) (**2b**).* Dark blue rod-like single crystals of **2a** transformed after 6 days into light blue block-like crystals of **2b** without any loss of crystallinity when immersed in a solution of **L3H** (1.0 M) in water/DMF (2:1, v/v) at RT. Yield: 2.15 g (74%). mp >290.15 °C. IR ν_{max} (ATR) (ν, cm^{-1}): 3041(s), 1609(sh), 1520(s), 1498(s), 1248(s), 1014(s). UV−vis λ_{max} (nm) (ε, M^{-1} cm^{-1}) ($CHCl_3$): 505 (740), 401 (4958), 318 (4365), 274 (4531). HRMS (ESI) (positive mode, m/z): calcd for $C_{28}H_{28}Br_2N_2O_2Cu$, 644.9814; found, 645.9782 ($[M + H]^+$). Anal. Calcd for $C_{28}H_{22}Br_2N_2O_2Cu$: (%) C, 52.40; H, 3.45; N, 4.36; Cu, 9.90. Found: C, 52.31; H, 3.39; N, 4.41; Cu, 9.51. μ_{eff} = 1.68 BM.

5.10. 2b → 2c CISA Transformation. *5.10.1. trans-Bis[2-({[4-(methyl)phenyl]imino-κN}methyl)-4-bromophenolato-κO]-nickel-(II) (**2c**).* Prior to direct metal exchange, the starting material was soaked in MeCN for 24 h to dissolve any remaining reactants that may be adhered to the precursor. During the process, MeCN was refreshed twice. Thereafter, the crystals of **2b** were dipped in the solution of the Ni^{II} acetate (0.5 M) in DMF/acetone (1:1, v/v) at RT. After 3 days, the solution was decanted, and the exchanged green block-like crystals obtained in 73% yield were finally washed thoroughly with a MeOH/water (1:2, v/v) mixture. A green powder of **2c** was also prepared via direct ligand exchange from **2a** under reflux at 70 °C for 12 h and was recrystallized from $CHCl_3$/acetone (1:4, v/v). Yield: 1.58 g (77%). mp >289.93 °C. IR ν_{max} (ATR) (ν, cm^{-1}): 3036(s), 1606(s), 1498(s), 1455(m), 1241(s), 1018(s). UV−vis λ_{max} (nm) (ε, M^{-1} cm^{-1}) ($CHCl_3$): 673 (98), 413 (2762), 358 (5860), 277 (5690). HRMS (ESI) (positive mode, m/z): calcd for $C_{28}H_{22}Br_2N_2O_2Ni$, 635.9381; found, 636.9355 ($[M + H]^+$). Anal. Calcd for $C_{28}H_{22}Br_2N_2O_2Ni$: (%) C, 52.80; H, 3.48; N, 4.40; Ni, 9.21. Found: C, 52.72; H, 3.40; N, 4.49; Ni, 9.06. μ_{eff} = 0.089 BM (diamagnetic).

5.11. Kinetic Studies. AAS tests at RT were carried out by withdrawing stoichiometric quantities (∼2 μL) from the reaction mixtures and diluting the samples 5-fold in deionized water. All the measurements were conducted at 12 h intervals, and the plots (in the Supporting Information) are presented between 0 and 180 h (or 0−7 days).

■ ASSOCIATED CONTENT

Supporting Information

The Supporting Information is available free of charge at https://pubs.acs.org/doi/10.1021/acs.cgd.3c00055.

Atomic numbering scheme and anisotropic displacement parameters for the ligands; crystallographic data; bond lengths and angles; crystal packing features; mass spectra (ESI-MS); {^1H + ^{13}C} NMR, IR, PXRD, and UV−vis spectra measurements; kinetic studies; and TG analysis curves (PDF)

Accession Codes

CCDC 1958580, 1989367, 2014924, 2020177, 2142833−2142835, and 2223008−2223012 contain the supplementary crystallographic data for this paper. These data can be obtained free of charge via www.ccdc.cam.ac.uk/data_request/cif, or by emailing data_request@ccdc.cam.ac.uk, or by contacting The Cambridge Crystallographic Data Centre, 12 Union Road, Cambridge CB2 1EZ, UK; fax: +44 1223 336033.

https://doi.org/10.1021/acs.cgd.3c00055
Cryst. Growth Des. 2023, 23, 4836−4854

AUTHOR INFORMATION

Corresponding Authors

Siya T. Hulushe − *Department of Chemistry, Rhodes University, Grahamstown 6139, South Africa;* orcid.org/0000-0002-1944-6155; Phone: (+27) 466-038-254; Email: hulushesiya@gmail.com

Frederick P. Malan − *Department of Chemistry, University of Pretoria, Pretoria 0002, South Africa*; Phone: (+27) 124-203-091; Email: frikkie.malan@gmail.com

Authors

Eric C. Hosten − *Department of Chemistry, Nelson Mandela University, Gqeberha, Port Elizabeth 6031, South Africa*

Matthew P. Akerman − *School of Chemistry and Physics, University of Kwa-Zulu Natal, Pietermaritzburg 3209, South Africa;* orcid.org/0000-0001-5116-488X

Andreas Lemmerer − *Molecular Sciences Institute, School of Chemistry, University of the Witwatersrand, 2050 Johannesburg, South Africa;* orcid.org/0000-0003-1569-2831

Setshaba D. Khanye − *Faculty of Pharmacy, Rhodes University, Grahamstown 6139, South Africa*

Gareth M. Watkins − *Department of Chemistry, Rhodes University, Grahamstown 6139, South Africa*

Complete contact information is available at: https://pubs.acs.org/10.1021/acs.cgd.3c00055

Author Contributions

The manuscript was written through contributions of all authors. All authors have given approval to the final version of the manuscript.

Notes

The authors declare no competing financial interest.

ACKNOWLEDGMENTS

The authors thank Dr. Maritjie Stander (Stellenbosch University, South Africa) of Central Analytical Facility (CAF) for mass spectrometry data. We would also want to express our gratitude to the anonymous reviewers, whose insightful comments assisted us in improving the paper. We are grateful to the National Research Foundation (NRF, South Africa), Atlantic Philanthropies Scholarship and Rhodes University Research Council, for the financial support.

ADDITIONAL NOTES

[a]CISA is related to transmetalation or cation exchange.
[b]LISA is associated with ligand substitution.

REFERENCES

(1) Mukherjee, P.; Drew, M. G. B.; Ghosh, A. Anion-directed template synthesis and hydrolysis of mono-condensed Schiff base of 1,3-pentanediamine and o-hydroxyacetophenone in Ni^{II} and Cu^{II} Complexes. *Eur. J. Inorg. Chem.* **2008**, *2008*, 3372−3381.

(2) Lewing, D.; Koppetz, H.; Hahn, F. E. Reversible Formation and Transmetalation of Schiff-Base Complexes in Subcomponent Self-Assembly Reactions. *Inorg. Chem.* **2015**, *54*, 7653−7659.

(3) Depree, C. V.; Beckmann, U.; Heslop, K.; Brooker, S. Monomeric, trimeric and polymeric assemblies of dicopper(II) complexes of a triazolate-containing Schiff-base macrocycle. *Dalton Trans.* **2003**, 3071−3081.

(4) Schick, J. W.; Hartough, H. D. Metalation studies in the thiophene series. II. Transmetalation of the alkylthiophenes. *J. Am. Chem. Soc.* **1948**, *70*, 1645−1648.

(5) Cheng, H. F.; Paul, M. K.; d'Aquino, A. I.; Stern, C. L.; Mirkin, C. A. Multi-State Dynamic Coordination Complexes Interconverted through Counterion-Controlled Phase Transfer. *Inorg. Chem.* **2021**, *60*, 4755−4763.

(6) Rasmussen, S. C. Transmetalation: a fundamental organometallic reaction critical to synthesis and catalysis. *ChemTexts* **2021**, *7*, 1−8.

(7) Mazzoni, R.; Roncaglia, F.; Rigamonti, L. When the Metal Makes the Difference: Template Syntheses of Tridentate and Tetradentate Salen-Type Schiff Base Ligands and Related Complexes. *Crystals* **2021**, *11*, 483.

(8) Ho, T.-Y.; Huang, S.-M.; Wu, J.-Y.; Hsu, K.-C.; Lu, K.-L. Direct guest exchange induced single-crystal to single-crystal transformation accompanying irreversible crystal expansion in soft porous coordination polymers. *Cryst. Growth Des.* **2015**, *15*, 4266−4271.

(9) He, Y.-C.; Yang, J.; Liu, Y.-Y.; Ma, J.-F. Series of Solvent-Induced Single-Crystal to Single-Crystal Transformations with Different Sizes of Solvent Molecules. *Inorg. Chem.* **2014**, *53*, 7527−7533.

(10) Wu, J.-Y.; Liu, Y.-C.; Chao, T.-C. From 1D Helix to 0D Loop: Nitrile Anion Induced Structural Transformation Associated with Unexpected N-Nitrosation of Amine Ligand. *Inorg. Chem.* **2014**, *53*, 5581−5588.

(11) Khullar, S.; Mandal, S. K. Supramolecular Assemblies of Dimanganese Subunits and Water Clusters Organized by Strong Hydrogen Bonding Interactions: Single Crystal to Single Crystal Transformation by Thermal De-/Rehydration Processes. *Cryst. Growth Des.* **2012**, *12*, 5329−5337.

(12) Yao, Q.; Sun, J.; Li, K.; Su, J.; Peskov, M. V.; Zou, X. A series of isostructural mesoporous metal−organic frameworks obtained by ion-exchange induced single-crystal to single-crystal transformation. *Dalton Trans.* **2012**, *41*, 3953−3955.

(13) Mobin, S. M.; Srivastava, A. K.; Mathur, P.; Lahiri, G. K. Single-crystal to single-crystal transformations in discrete hydrated dimeric copper complexes. *Dalton Trans.* **2010**, *39*, 1447−1449.

(14) Reinoso, S.; Artetxe, B.; Gutiérrez-Zorrilla, J. M. Single-crystal-to-single-crystal transformations triggered by dehydration in polyoxometalate-based compounds. *Acta Crystallogr., Sect. C: Struct. Chem.* **2018**, *74*, 1222−1242.

(15) Chaudhary, A.; Mohammad, A.; Mobin, S. M. Recent Advances in Single-Crystal-to-Single-Crystal Transformation at the Discrete Molecular Level. *Cryst. Growth Des.* **2017**, *17*, 2893−2910.

(16) Jacobs, T.; Barbour, L. J. Single-crystal to single-crystal transformations in discrete solvated metallocycles: the role of the metal ion. *New J. Chem.* **2013**, *37*, 71−74.

(17) Barry, K.-L.; Grimmer, C. D.; Munro, O. Q.; Akerman, M. P. Self-assembled supramolecular structures of O,N,N'-tridentate imidazole-phenol Schiff base compounds. *RSC Adv.* **2020**, *10*, 7867−7878.

(18) Spessard, G. O.; Miessler, G. L. *Organic Chemistry*; Oxford University Press: New York, NY, 2010.

(19) Gradinaru, J.; Forni, A.; Druta, V.; Tessore, F.; Zecchin, S.; Quici, S.; Garbalau, N. Structural, Spectral, Electric-Field-Induced Second Harmonic, and Theoretical Study of Ni(II), Cu(II), Zn(II), and VO(II) Complexes with $[N_2O_2]$ Unsymmetrical Schiff Bases of S-Methylisothiosemicarbazide Derivatives. *Inorg. Chem.* **2007**, *46*, 884−895.

(20) Sharma, V.; Piwnica-Worms, D. Metal Complexes for Therapy and Diagnosis of Drug Resistance. *Chem. Rev.* **1999**, *99*, 2545−2560.

(21) Cozzi, P. G. Metal-Salen Schiff base complexes in catalysis: practical aspects. *Chem. Soc. Rev.* **2004**, *33*, 410−421.

(22) Liu, X. H.; Lin, L.; Feng, X. M. Chiral N,N'-Dioxides: New Ligands and Organocatalysts for Catalytic Asymmetric Reactions. *Acc. Chem. Res.* **2011**, *44*, 574−587.

(23) Han, Y.; Chilton, N. F.; Li, M.; Huang, C.; Xu, H.; Hou, H.; Moubaraki, B.; Langley, S. K.; Batten, S. R.; Fan, Y.; Murray, K. S. Post-Synthetic Monovalent Central-Metal Exchange, Specific I_2 Sensing, and Polymerization of a Catalytic [3x3] Grid of $[Cu^{II}_5Cu^{I}_4L_6]\cdot(I)_2\cdot 13H_2O$. *Chem.—Eur. J.* **2013**, *19*, 6321−6328.

(24) Liu, M.; Zhang, L.; Wang, T. Supramolecular Chirality in Self-Assembled Systems. *Chem. Rev.* **2015**, *115*, 7304−7397.

(25) Galley, S. S.; Pattenaude, S. A.; Gaggioli, C. A.; Qiao, Y.; Sperling, J. M.; Zeller, M.; Pakhira, S.; Mendoza-Cortes, J. L.; Schelter, E. J.; Albrecht-Schmitt, T. E.; Gagliardi, L.; Bart, S. C. Synthesis and Characterization of Tris-chelate Complexes for Understanding f-Orbital Bonding in Later Actinides. *J. Am. Chem. Soc.* **2019**, *141*, 2356−2366.
(26) Lin, Z. J.; Lü, J.; Hong, M.; Cao, R. Metal−organic frameworks based on flexible ligands (FL-MOFs): structures and applications. *Chem. Rev.* **2014**, *43*, 5867−5895.
(27) Nakanishi, H.; Jones, W.; Thomas, J. M. Topochemical single-crystal-to-single-crystal photodimerization. *Chem. Phys. Lett.* **1980**, *71*, 44−48.
(28) Cheansirisomboon, A.; Pakawatchai, C.; Youngme, S. Solvent-Induced Reversible Crystal-to-Amorphous Transformation Properties of Cobalt(II) 4-Aminomethylpyridine-Sulfate with Chromotropism. *Aust. J. Chem.* **2013**, *66*, 477−484.
(29) Boonmak, J.; Nakano, M.; Chaichit, N.; Pakawatchai, C.; Youngme, S. Water-induced reversible structural phase transformation with chromotropism in metal supramolecular frameworks containing aminopyrazine and sulfate anions. *Dalton Trans.* **2010**, *39*, 8161−8167.
(30) Narang, S.; Singh, U. P.; Venugopalan, P. Solvent-mediated supramolecular templated assembly of a metal organophosphonate via a crystal−amorphous−crystal transformation. *CrystEngComm* **2016**, *18*, 54−61.
(31) Garai, M.; Biradha, K. Coordination polymers of organic polymers synthesised via photopolymerization of single crystals: two-dimensional hydrogen bonding layers with amazing shock absorbing nature. *Chem. Commun.* **2014**, *50*, 3568−3570.
(32) He, Y.-C.; Kan, W.-Q.; Guo, J.; Yang, Y.; Du, P.; Liu, Y.-Y.; Ma, J.-F. Iodine-templated assembly of an In(III) complex with a single-crystal-to-single-crystal transition. *CrystEngComm* **2013**, *15*, 7406−7409.
(33) Martí-Rujas, J.; Bonafede, S.; Tushi, D.; Cametti, M. Multiple single-crystal-to-single-crystal guest exchange in a dynamic 1D coordination polymer. *Chem. Commun.* **2015**, *51*, 12357−12360.
(34) Kyprianidou, E. J.; Lazarides, T.; Kaziannis, S.; Kosmidis, C.; Itskos, G.; Manos, M. J.; Tasiopoulos, A. J. Single crystal coordinating solvent exchange as a general method for the enhancement of the photoluminescence properties of lanthanide MOFs. *J. Mater. Chem. A* **2014**, *2*, 5258−5266.
(35) Zhang, X.; Vieru, V.; Feng, X.; Liu, J.-L.; Zhang, Z.; Na, B.; Shi, W.; Wang, B.-W.; Powell, A. K.; Chibotaru, L. F.; Gao, S.; Cheng, P.; Long, J. R. Influence of Guest Exchange on the Magnetization Dynamics of Dilanthanide Single-Molecule-Magnet Nodes within a Metal−Organic Framework. *Angew. Chem., Int. Ed.* **2015**, *54*, 9861−9865.
(36) Marshall, R. J.; Griffin, S. L.; Wilson, C.; Forgan, R. S. Single-Crystal to Single-Crystal Mechanical Contraction of Metal−Organic Frameworks through Stereoselective Postsynthetic Bromination. *J. Am. Chem. Soc.* **2015**, *137*, 9527−9530.
(37) Park, I.-H.; Chanthapally, A.; Lee, H.-H.; Quah, H. S.; Lee, S. S.; Vittal, J. J. Solid-state conversion of a MOF to a metal-organo polymeric framework (MOPF) via [2+2] cycloaddition reaction. *Chem. Commun.* **2014**, *50*, 3665−3667.
(38) Li, J.; Huang, P.; Wu, X.-R.; Tao, J.; Huang, R.-B.; Zheng, L.-S. Metal-organic frameworks displaying single crystal-to-single crystal transformation through postsynthetic uptake of metal clusters. *Chem. Sci.* **2013**, *4*, 3232−3238.
(39) Nagarathinam, M.; Peedikakkal, A. M. P.; Vittal, J. J. Stacking of double bonds for photochemical [2+2] cycloaddition reactions in the solid state. *Chem. Commun.* **2008**, 5277−5288.
(40) Medishetty, R.; Park, I.-H.; Lee, S. S.; Vittal, J. J. Solid-state polymerisation via [2+2] cycloaddition reaction involving coordination polymers. *Chem. Commun.* **2016**, *52*, 3989−4001.
(41) Liu, H.-K.; Tsao, T.-H.; Zhang, Y.-T.; Lin, C.-H. Microwave synthesis and single-crystal-to-single-crystal transformation of magnesium coordination polymers exhibiting selective gas adsorption and luminescence properties. *CrystEngComm* **2009**, *11*, 1462−1468.
(42) Toh, N. L.; Nagarathinam, M.; Vittal, J. J. Topochemical Photodimerization in the Coordination Polymer $[\{(CF_3CO_2)(\mu\text{-}O_2CCH_3)Zn\}_2(\mu\text{-bpe})_2]_n$ through Single-Crystal to Single-Crystal Transformation. *Angew. Chem., Int. Ed.* **2005**, *44*, 2237−2241.
(43) Choi, H. J.; Suh, M. P. Dynamic and Redox Active Pillared Bilayer Open Framework: Single-Crystal-to-Single-Crystal Transformations upon Guest Removal, Guest Exchange, and Framework Oxidation. *J. Am. Chem. Soc.* **2004**, *126*, 15844−15851.
(44) Suh, M. P.; Ko, J. W.; Choi, H. J. A Metal−Organic Bilayer Open Framework with a Dynamic Component: Single-Crystal-to-Single-Crystal Transformations. *J. Am. Chem. Soc.* **2002**, *124*, 10976−10977.
(45) Shen, P.; He, W.-W.; Du, D.-Y.; Jiang, H.-L.; Li, S.-L.; Lang, Z. L.; Su, Z.-M.; Fu, Q.; Lan, Y.-Q. Solid-state structural transformation doubly triggered by reaction temperature and time in 3D metal-organic frameworks: great enhancement of stability and gas adsorption. *Chem. Sci.* **2014**, *5*, 1368−1374.
(46) Hu, F. l.; Shi, Y.-X.; Chen, H.-H.; Lang, J.-P. A Zn(II) coordination polymer and its photocycloaddition product: syntheses, structures, selective luminescence sensing of iron(III) ions and selective absorption of dyes. *Dalton Trans.* **2015**, *44*, 18795−18803.
(47) Lee, E. Y.; Suh, M. P. A Robust Porous Material Constructed of Linear Coordination Polymer Chains: Reversible Single-Crystal to Single-Crystal Transformations upon Dehydration and Rehydration. *Angew. Chem., Int. Ed.* **2004**, *43*, 2798−2801.
(48) Choi, S. B.; Furukawa, H.; Nam, H. J.; Jung, D. Y.; Jhon, Y. H.; Walton, A.; Book, D.; O'Keeffe, M.; Yaghi, O. M.; Kim, J. Reversible Interpenetration in a Metal−Organic Framework Triggered by Ligand Removal and Addition. *Angew. Chem., Int. Ed.* **2012**, *51*, 8791−8795.
(49) Zhang, T.; Lu, Y.; Zhang, Z.; Lan, Q.; Liu, D.; Wang, E. Single-crystal to single-crystal transformation from a hydrophilic−hydrophobic metal−organic framework to a layered coordination polymer. *Inorg. Chim. Acta* **2014**, *411*, 128−133.
(50) Zhang, S.; Qu, X. N.; Xie, G.; Wei, Q.; Chen, S.-P. Syntheses, structural analyses and luminescent property of four alkaline-earth coordination polymers. *J. Solid State Chem.* **2014**, *210*, 36−44.
(51) Lee, E.; Kim, Y.; Heo, J.; Park, K.-M. 3D Metal−Organic Framework Based on a Lower-Rim Acid-Functionalized Calix[4]-arene: Crystal-to-Crystal Transformation upon Lattice Solvent Removal. *Cryst. Growth Des.* **2015**, *15*, 3556−3560.
(52) Nanthamathee, C.; Ling, S.; Slater, B.; Attfield, M. P. Contradistinct Thermoresponsive Behavior of Isostructural MIL-53 Type Metal−Organic Frameworks by Modifying the Framework Inorganic Anion. *Chem. Mater.* **2015**, *27*, 85−95.
(53) Férey, G.; Serre, C. Large breathing effects in three-dimensional porous hybrid matter: facts, analyses, rules and consequences. *Chem. Soc. Rev.* **2009**, *38*, 1380−1399.
(54) Min, K. S.; Suh, M. P. Silver(I)−Polynitrile Network Solids for Anion Exchange: Anion-Induced Transformation of Supramolecular Structure in the Crystalline State. *J. Am. Chem. Soc.* **2000**, *122*, 6834−6840.
(55) Das, M. C.; Bharadwaj, P. K. A Porous Coordination Polymer Exhibiting Reversible Single-Crystal to Single-Crystal Substitution Reactions at Mn(II) Centers by Nitrile Guest Molecules. *J. Am. Chem. Soc.* **2009**, *131*, 10942−10949.
(56) Jung, O.-S.; Kim, Y. J.; Lee, Y.-A.; Park, J. K.; Chae, H. K. Smart Molecular Helical Springs as Tunable Receptors. *J. Am. Chem. Soc.* **2000**, *122*, 9921−9925.
(57) Cangelosi, V. M.; Zakharov, L. N.; Johnson, D. W. Supramolecular "Transmetalation" Leads to an Unusual Self-Assembled P_2L_3 Cryptand. *Angew. Chem., Int. Ed.* **2010**, *49*, 1248−1251.
(58) Escudero-Adan, E. C.; Benet-Buchholz, J.; Kleij, A. W. Expedient Method for the Transmetalation of Zn(II)-Centered Salphen Complexes. *Inorg. Chem.* **2007**, *46*, 7265−7267.
(59) Dömer, J.; Slootweg, J. C.; Hupka, F.; Lammertsma, K.; Hahn, F. E. Subkomponenten-Selbstorganisation und Transmetallierung zweikerniger Helikate. *Angew. Chem., Int. Ed.* **2010**, *49*, 6430.

https://doi.org/10.1021/acs.cgd.3c00055
Cryst. Growth Des. 2023, 23, 4836−4854

(60) Szilágyi, P. Á.; Serra-Crespo, P.; Dugulan, I.; Gascon, J.; Geerlings, H.; Dam, B. Post-synthetic cation exchange in the robust metal−organic framework MIL-101(Cr). *CrystEngComm* **2013**, *15*, 10175−10178.
(61) Evans, J. D.; Sumby, C. J.; Doonan, C. J. Post-synthetic metalation of metal−organic frameworks. *Chem. Soc. Rev.* **2014**, *43*, 5933−5951.
(62) Wang, H.; Meng, W.; Wu, J.; Ding, J.; Hou, H.; Fan, Y. Crystalline central-metal transformation in metal-organic frameworks. *Coord. Chem. Rev.* **2016**, *307*, 130−146.
(63) Mukherjee, G.; Biradha, K. Post-synthetic modification of isomorphic coordination layers: exchange dynamics of metal ions in a single crystal to single crystal fashion. *Chem. Commun.* **2012**, *48*, 4293−4295.
(64) Huang, C.; Wang, Y.; Wei, C.; Li, N.; Ji, F.; Wu, J.; Hou, H. Cation-exchange-induced single-crystal-to-single-crystal transformations of a nanoporous coordination complex. *Inorg. Chem. Commun.* **2013**, *32*, 68−73.
(65) Basak, D.; Leusen, J. v.; Gupta, T.; Kögerler, P.; Bertolasi, V.; Ray, D. Unusually Distorted Pseudo-Octahedral Coordination Environment Around Co^{II} from Thioether Schiff Base Ligands in Dinuclear [CoLn] (Ln = La, Gd, Tb, Dy, Ho) Complexes: Synthesis, Structure, and Understanding of Magnetic Behavior. *Inorg. Chem.* **2020**, *59*, 2387−2405.
(66) Wu, J.-Y.; Chang, C.-Y.; Tsai, C.-J.; Lee, J.-J. Reversible Single-Crystal to Single-Crystal Transformations of a Zn(II)−Salicyaldimine Coordination Polymer Accompanying Changes in Coordination Sphere and Network Dimensionality upon Dehydration and Rehydration. *Inorg. Chem.* **2015**, *54*, 10918−10924.
(67) Wu, J.-Y.; Tsai, C.-J.; Chang, C.-Y.; Wu, Y.-Y. Metal-ion exchange induced structural transformation as a way of forming novel Ni(II)− and Cu(II)−salicylaldimine structures. *J. Solid State Chem.* **2017**, *246*, 23−28.
(68) Li, N.; Jiang, F.; Chen, L.; Li, X.; Chen, Q.; Hong, M. From discrete octahedral nanocages to 1D coordination polymer: Coordination-driven a single-crystal-to-single-crystal transformation via anion exchange. *Chem. Commun.* **2011**, *47*, 2327−2329.
(69) Wang, X.; Zhang, H.; Sinkler, W.; Poeppelmeier, K. R.; Marks, L. D. Reduction of magnesium orthovanadate $Mg_3(VO_4)_2$. *J. Alloys Compd.* **1998**, *270*, 88−94.
(70) Iordanidis, L.; Kanatzidis, M. G. Redox-Induced "Zipper" Action in the Solid State. Unprecedented Single-Crystal to Single-Crystal to Single-Crystal Cascade Conversions in $Cs_3Bi_7Se_{12}$. Framework Evolution from 2D to 2D' to 3D. *J. Am. Chem. Soc.* **2000**, *122*, 8319−8320.
(71) Iordanidis, L.; Kanatzidis, M. G. Redox-Induced "Zipper" Action in $Rb_2Bi_4Se_7$ and $Cs_2Bi_4Se_7$: Coupling of Slabs to a Three-Dimensional Framework through Single-Crystal to Single-Crystal Conversion. *Angew. Chem., Int. Ed.* **2000**, *39*, 1927−1930.
(72) Crabtree, R. H. *The Organometallic Chemistry of the Transition Metals*, 6th ed.; Wiley: Hoboken, 2014.
(73) Kochem, A.; Carrillo, A.; Philouze, C.; van Gastel, M.; du Moulinet d'Hardemare, A.; Thomas, F. Copper(II)-Coordinated α-Azophenols: Effect of the Metal-Ion Geometry on Phenoxyl/Phenolate Oxidation Potential and Reactivity. *Eur. J. Inorg. Chem.* **2014**, *2014*, 4263−4267.
(74) Muthuramalingam, S.; Anandababu, K.; Velusamy, M.; Mayilmurugan, R. Benzene Hydroxylation by Bioinspired Copper(II) Complexes: Coordination Geometry versus Reactivity. *Inorg. Chem.* **2020**, *59*, 5918−5928.
(75) Combariza, M. Y.; Vachet, R. W. Effect of Coordination Geometry on the Gas-Phase Reactivity of Four-Coordinate Divalent Metal Ion Complexes. *J. Phys. Chem. A* **2004**, *108*, 1757−1763.
(76) Shang, X.; Yue, X.; Chen, Y.; Li, C.; Chen, H.; Wang, T. Design, synthesis, crystal structure and cytotoxicity studies of colorimetric fluorescent "OFF-ON" probes for rapid detection of hydrogen sulfide based on Cu(II) complex. *Inorg. Chem. Commun.* **2019**, *99*, 1−10.
(77) Allen, F. H. The Cambridge Structural Database: a quarter of a million crystal structures and rising. *Acta Crystallogr., Sect. B: Struct. Sci.* **2002**, *58*, 380−388.
(78) Groom, C. R.; Bruno, I. J.; Lightfoot, M. P.; Ward, S. C. The Cambridge Structural Database. *Acta Crystallogr., Sect. B: Struct. Sci., Cryst. Eng. Mater.* **2016**, *72*, 171−179.
(79) Hulushe, S. T.; Malan, F. P.; Hosten, E. C.; Lobb, K. A.; Khanye, S. D.; Watkins, G. M. Photo-and thermoresponsive N-salicylideneaniline derivatives: solid-state studies and structural aspects. *New J. Chem.* **2022**, *46*, 20940−20950.
(80) Cho, J.; Lough, A. J.; Kim, J. C. Monomeric and polymeric copper(II) hexaaza macrocyclic complexes with btc anions (btc =1,2,4,5-benzenetetracarboxylic acid). *Inorg. Chim. Acta* **2003**, *342*, 305−310.
(81) Nithya, P.; Simpson, J.; Govindarajan, S. Template synthesis, structural variation, thermal behavior and antimicrobial screening of Mn(II), Co(II) and Ni(II) complexes of Schiff base ligands derived from benzyl carbazate and three isomers of acetylpyridine. *Inorg. Chim. Acta* **2017**, *467*, 180−193.
(82) Lever, A. B. P. *Inorganic Electronic Spectroscopy*; Elsevier, 1968.
(83) Tedim, J.; Patrício, S.; Bessada, R.; Morais, R.; Sousa, C.; Marques, M. B.; Freire, C. Third-Order Nonlinear Optical Properties of DA-salen-Type Nickel(II) and Copper(II) Complexes. *Eur. J. Inorg. Chem.* **2006**, *2006*, 3425−3433.
(84) Halcrow, M. A. Jahn−Teller distortions in transition metal compounds, and their importance in functional molecular and inorganic materials. *Chem. Soc. Rev.* **2013**, *42*, 1784−1795.
(85) Lee, E.; Lee, S. S. Syntheses and Crystal Structures of Mercury(II) and Copper(II) Complexes of an 18-Membered NS_4-Macrocycle. *Bull. Korean Chem. Soc.* **2015**, *36*, 36−42.
(86) Dutta, G.; Jana, A. K.; Natarajan, S. Assembling Porphyrins into Extended Network Structures by Employing Aromatic Dicarboxylates: Synthesis, Metal Exchange, and Heterogeneous Catalytic Studies. *Chem.—Eur. J.* **2017**, *23*, 8932−8940.
(87) Jana, B.; Cera, L.; Akhuli, B.; Naskar, S.; Schalley, C. A.; Ghosh, P. Competitive Transmetalation of First-Row Transition-Metal Ions between Trinuclear Triple-Stranded Side-by-Side Helicates. *Inorg. Chem.* **2017**, *56*, 12505−12513.
(88) Flack, H. D. On enantiomorph-polarity estimation. *Acta Crystallogr., Sect. A: Found. Crystallogr.* **1983**, *39*, 876−881.
(89) Mrutu, A.; Lane, A. C.; Drewett, J. M.; Yourstone, S. D.; Barnes, C. L.; Halsey, C. M.; Cooley, J. W.; Walensky, J. R. Molecular structure and spectroscopy of divalent first row transition metals, Mn−Zn, with salicylaldiminate ligands. *Polyhedron* **2013**, *54*, 300−308.
(90) Yang, L.; Powell, D. R.; Houser, R. P. Structural variation in copper(I) complexes with pyridylmethylamide ligands: structural analysis with a new four-coordinate geometry index τ_4. *Dalton Trans.* **2007**, 955−964.
(91) Saini, A. K.; Saraf, M.; Kumari, P.; Mobin, S. M. A highly selective and sensitive chemosensor for L-tryptophan by employing a Schiff based Cu(II) complex. *New J. Chem.* **2018**, *42*, 3509−3518.
(92) Kani, Y.; Ohba, S.; Ishikawa, T.; Sakamoto, M.; Nishida, Y. {2-[2-(Salicylideneaminomethyl)phenylimino-methyl]phenolato(2−)-N,N',O,O'}copper(II). *Acta Crystallogr., Sect. C: Cryst. Struct. Commun.* **1998**, *54*, 191−193.
(93) Lo, J.-M.; Yao, H.-H.; Liao, F.-L.; Wang, S.-L.; Lu, T.-H. [N,N'-Bis(salicylidene)-1,2-diimino-2-methylpropane]copper(II). *Acta Crystallogr., Sect. C: Cryst. Struct. Commun.* **1997**, *53*, 848−850.
(94) Connor, E. F.; Younkin, T. R.; Henderson, J. I.; Waltman, A. W.; Grubbs, R. H. Synthesis of neutral nickel catalysts for ethylenepolymerization − the influence of ligand size on catalyst stability. *Chem. Commun.* **2003**, 2272−2273.
(95) Ölscher, F.; Göttker-Schnetmann, I.; Monteil, V.; Mecking, S. Role of Radical Species in Salicylaldiminato Ni(II) Mediated Polymer Chain Growth: A Case Study for the Migratory Insertion Polymerization of Ethylene in the Presence of Methyl Methacrylate. *J. Am. Chem. Soc.* **2015**, *137*, 14819−14828.

https://doi.org/10.1021/acs.cgd.3c00055
Cryst. Growth Des. 2023, 23, 4836−4854

(96) Song, X.; Wang, Z.; Zhao, J.; Hor, T. S. A. Sodium cubane and double-cubane aggregates of hybridised salicylaldimines and their transmetallation to nickel for catalytic ethylene oligomerisation. *Chem. Commun.* **2013**, *49*, 4992−4994.
(97) Khandar, A. A.; Hosseini-Yazdi, S. A.; Zarei, S. A. Synthesis, characterization and X−ray crystal structures of copper(II) and nickel(II) complexes with potentially hexadentate Schiff base ligands. *Inorg. Chim. Acta* **2005**, *358*, 3211−3217.
(98) Jurca, T.; Ouanounou, S.; Shih, W.-C.; Ong, T.-G.; Yap, G. P. A.; Korobkov, I.; Gorelsky, S.; Richeson, D. Structural and electronic trends for five coordinate 1st row transition metal complexes: Mn(II) to Zn(II) captured in a bis(iminopyridine) framework. *Dalton Trans.* **2016**, *45*, 14327−14334.
(99) Rigaku. *Rigaku Oxford Diffraction*; Rigaku Corporation: Oxford, UK, 2018.
(100) Bruker. *SAINT (Version 7.68A)*; Bruker-AXS Inc.: Madison, Wisconsin, USA, 2012.
(101) Bruker. *APEX-II (2011.4-1) and SADABS (Version 2008/1)*; Bruker AXS Inc.: Madison, Wisconsin, USA, 2012.
(102) Sheldrick, G. M. SHELXT− Integrated space-group and crystal-structure determination. *Acta Crystallogr., Sect. A: Found. Adv.* **2015**, *71*, 3−8.
(103) Dolomanov, O. V.; Bourhis, L. J.; Gildea, R. J.; Howard, J. A. K.; Puschmann, H. OLEX2: a complete structure solution, refinement and analysis program. *J. Appl. Crystallogr.* **2009**, *42*, 339−341.
(104) Bourhis, L. J.; Dolomanov, O. V.; Gildea, R. J.; Howard, J. A. K.; Puschmann, H. The anatomy of a comprehensive constrained, restrained refinement program for the modern computing environment − Olex2 dissected. *Acta Crystallogr., Sect. A: Found. Adv.* **2015**, *71*, 59−75.
(105) Sheldrick, G. M. Crystal structure refinement with SHELXL. *Acta Crystallogr., Sect. C: Struct. Chem.* **2015**, *71*, 3−8.
(106) Sheldrick, G. M. *SHELXL-97, Program for the Refinement of Crystal Structures*; University of Göttingen: Germany, 1997.
(107) Spek, A. L. Structure validation in chemical crystallography. *Acta Crystallogr., Sect. D: Biol. Crystallogr.* **2009**, *65*, 148−155.
(108) Spek, A. L. Single-crystal structure validation with the programPLATON. *J. Appl. Crystallogr.* **2003**, *36*, 7−13.
(109) Macrae, C. F.; Edgington, P. R.; McCabe, P.; Pidcock, E.; Shields, G. P.; Taylor, R.; Towler, M.; van de Streek, J. Mercury: visualization and analysis of crystal structures. *J. Appl. Crystallogr.* **2006**, *39*, 453−457.
(110) Barbour, L. J. X-Seed − A software tool for supramolecular crystallography. *J. Supramol. Chem.* **2001**, *1*, 189−191.
(111) Allen, F. H.; Johnson, O.; Shields, G. P.; Smith, B. R.; Towler, M. CIF applications. XV. enCIFer: a program for viewing, editing and visualizing CIFs. *J. Appl. Crystallogr.* **2004**, *37*, 335−338.
(112) Becke, A. D. Density-functional thermochemistry. III. The role of exact exchange. *J. Chem. Phys.* **1993**, *98*, 5648−5652.
(113) Lee, C.; Yang, W.; Parr, R. G. Development of the Colle-Salvetti correlation-energy formula into a functional of the electron density. *Phys. Rev. B: Condens. Matter Mater. Phys.* **1988**, *37*, 785−789.
(114) Frisch, M. J.; Trucks, G. W.; Schlegel, H. B.; Scuseria, G. E.; Robb, M. A.; Cheeseman, J. R.; Scalmani, G.; Barone, V.; Petersson, G. A.; Nakatsuji, H.; Li, X.; Caricato, M.; Marenich, A. V.; Bloino, J.; Janesko, B. G.; Gomperts, R.; Mennucci, B.; Hratchian, H. P.; Ortiz, J. V.; Izmaylov, A. F.; Sonnenberg, J. L.; Williams-Young, D.; Ding, F.; Lipparini, F.; Egidi, F.; Goings, J.; Peng, B.; Petrone, A.; Henderson, T.; Ranasinghe, D.; Zakrzewski, V. G.; Gao, J.; Rega, N.; Zheng, G.; Liang, W.; Hada, M.; Ehara, M.; Toyota, K.; Fukuda, R.; Hasegawa, J.; Ishida, M.; Nakajima, T.; Honda, Y.; Kitao, O.; Nakai, H.; Vreven, T.; Throssell, K.; Montgomery, J. A., Jr.; Peralta, J. E.; Ogliaro, F.; Bearpark, M. J.; Heyd, J. J.; Brothers, E. N.; Kudin, K. N.; Staroverov, V. N.; Keith, T. A.; Kobayashi, R.; Normand, J.; Raghavachari, K.; Rendell, A. P.; Burant, J. C.; Iyengar, S. S.; Tomasi, J.; Cossi, M.; Millam, J. M.; Klene, M.; Adamo, C.; Cammi, R.; Ochterski, J. W.; Martin, R. L.; Morokuma, K.; Farkas, O.; Foresman, J. B.; Fox, D. J. *Gaussian 16*, Revision C.01; Gaussian, Inc.: Wallingford CT, 2016.
(115) Weigend, F.; Ahlrichs, R. Balanced basis sets of split valence, triple zeta valence and quadruple zeta valence quality for H to Rn: design and assessment of accuracy. *Phys. Chem. Chem. Phys.* **2005**, *7*, 3297−3305.
(116) Marenich, A. V.; Cramer, C. J.; Truhlar, D. G. Universal solvation model based on solute electron density and on a continuum model of the solvent defined by the bulk dielectric constant and atomic surface tensions. *J. Phys. Chem. B* **2009**, *113*, 6378−6396.
(117) Skyner, R. E.; Mcdonagh, J. L.; Groom, C. R.; van Mourik, T.; Mitchell, J. B. O. A review of methods for the calculation of solution free energies and the modelling of systems in solution. *Phys. Chem. Chem. Phys.* **2015**, *17*, 6174−6191.
(118) Chemcraft − graphical software for visualization of quantum chemistry computations. https://www.chemcraftprog.com (accessed June 2022).
(119) Zhong-Tao, J.; Liesegang, J.; James, B. D.; Skelton, B. W.; White, A. H. Atomic charges and structures of some hydrogen bonded substituted anilinium chloride systems: Correlation with XPS. *J. Phys. Chem. Solids* **1996**, *57*, 397−404.

NOTE ADDED AFTER ASAP PUBLICATION

In the first paragraph that discusses Figure 4, the Flack parameter was corrected from 0.037(8) to 0.019(10), the correct version reposted on June 7, 2023.

https://doi.org/10.1021/acs.cgd.3c00055
Cryst. Growth Des. 2023, 23, 4836−4854